

**CASE FILE
COPY**

N 62 70092

NASA MEMO 12-21-58L

NASA MEMO 12-21-58L

1N-02

394628

NASA

MEMORANDUM

THE TOTAL-PRESSURE RECOVERY AND DRAG CHARACTERISTICS
OF SEVERAL AUXILIARY INLETS AT TRANSONIC SPEEDS

By John S. Dennard

Langley Research Center
Langley Field, Va.

**NATIONAL AERONAUTICS AND
SPACE ADMINISTRATION**

WASHINGTON

March 1959

Declassified September 1, 1959

NATIONAL AERONAUTICS AND SPACE ADMINISTRATION

MEMORANDUM 12-21-58L

THE TOTAL-PRESSURE RECOVERY AND DRAG CHARACTERISTICS
OF SEVERAL AUXILIARY INLETS AT TRANSONIC SPEEDS*

By John S. Dennard

SUMMARY

Several flush and scoop-type auxiliary inlets have been tested for a range of Mach numbers from 0.55 to 1.3 to determine their transonic total-pressure recovery and drag characteristics. The inlet dimensions were comparable with the thickness of the boundary layer in which they were tested. Results indicate that flush inlets should be inclined at very shallow angles with respect to the surface for optimum total-pressure recovery and drag characteristics.

Deep, narrow inlets have lower drag than wide shallow ones at Mach numbers greater than 0.9 but at lower Mach numbers the wider inlets proved superior. Inlets with a shallow approach ramp, 7° , and diverging ramp walls which incorporated boundary-layer bypass had lower drag than any other inlet tested for Mach numbers up to 1.2 and had the highest pressure recovery of all of the flush inlets.

The scoop inlets, which operated in a higher velocity flow than the flush inlets, had higher drag coefficients.

Several of these auxiliary inlets projected multiple, periodic shock waves into the stream when they were operated at low mass-flow ratios.

INTRODUCTION

The amount of auxiliary equipment which requires cooling together with the air-flow requirements for cabin ventilation has increased auxiliary air-flow requirements to a point where they are an appreciable percentage of the main engine air-flow requirements. One method of

*Title, Unclassified.

supplying these auxiliary needs is to bleed the required auxiliary air flow from the main engine air diffuser. This method will generally provide high-pressure air but also requires that the main air inlet and the entire duct system be larger than it would be for engine air requirements alone. The problems of optimum total-pressure recovery, distortion, and flow stability may also be aggravated when the auxiliary air is bled from the engine duct. A second method of supplying auxiliary air is to provide separate air inlets for the accessories which require cooling and for ventilation. This method, which generally simplifies design of the main engine air system, will generally decrease the ducting required since the auxiliary inlet can be located close to the place where the air is needed. One disadvantage of such multiple small inlets is that they are of the same general dimensions as the boundary layer and may have poor pressure recovery characteristics.

The drag characteristics of open nose or scoop inlets, which are large compared to the approaching boundary layer, are comparatively well documented; however, the experimental drag characteristics of the smaller, auxiliary inlets are almost completely unavailable except at very low speeds (ref. 1). Transonic pressure recovery characteristics of several auxiliary inlets may be found in references 2, 3, and 4. Charts of boundary-layer mass flow and momentum are available in reference 5 from which ideal auxiliary-inlet performance may be obtained. No experimental information is available, however, whereby the transonic drag of auxiliary inlets may be determined for a body having a flat pressure distribution. The present paper has been prepared to present the transonic drag characteristics of several auxiliary inlets which have dimensions of the same order as the thickness of the boundary layer. The data presented supplement those of reference 4.

Of the 14 inlets investigated, 11 were flush and 3 were scoop-type inlets. One of the flush inlets had protuberances in the form of boundary-layer fences and one flush inlet used bypass ramps for boundary-layer control. The Mach number range was from 0.55 to 1.3 and both drag and total-pressure-recovery data are presented as a function of mass-flow ratio.

SYMBOLS

A	cross-sectional area of inlet, sq ft
a	velocity of sound, ft/sec
$C_{D,corr}$	corrected drag coefficient, $\frac{D_{corr}}{qA}$

$C_{D,N}$	net drag coefficient, $\frac{D_N}{qA}$
d	hydraulic diameter, $\frac{4A}{\text{Perimeter}}$
D_{corr}	corrected drag force, Net drag - Available thrust of inducted air, lb
D_N	net drag force, Measured drag - Tare drag, lb
H	total pressure, lb/sq ft
l	center-line length of inlet duct (constant area), in.
M	Mach number, $\frac{U}{a}$
$\frac{m_i}{m_\infty}$	ratio of mass flow through inlet to that in a free-stream tube of equal area
n	boundary-layer-profile exponent as given in $\frac{u}{U} = \left(\frac{y}{\delta}\right)^{\frac{1}{n}}$
p	static pressure, lb/sq ft
Δp	static-pressure differential, $p_\infty - p_i$, lb/sq ft
q_∞	free-stream dynamic pressure, $\frac{\gamma}{2} p_\infty M_\infty^2$, lb/sq ft
u	local velocity in boundary layer, ft/sec
U	free-stream velocity, ft/sec
X	distance measured downstream from inlet lip, in.
Y	depth of inlet ramp, in.
y	distance measured from surface to point of local velocity u , in boundary layer, in.
Z	half-width of inlet ramp, in.
γ	ratio of specific heats, 1.4

δ boundary-layer thickness measured to point where $\frac{u}{U} = 1.0$, in.

θ inclination angle of inlet axis, deg;

ϕ ramp angle, deg

Subscripts:

corr corrected drag or drag coefficient

N net drag or drag coefficient

i inlet conditions, measured at downstream end of constant-area throat

∞ free-stream conditions, measured outside of boundary layer

APPARATUS AND METHOD

The general arrangement of the flow system is shown in the line drawing of figure 1. Air is supplied to the tunnel entrance bell at a maximum pressure of 2 atmospheres absolute without benefit of aftercooling or drying. From the entrance bell the air flows through a $4\frac{1}{2}$ - by $6\frac{1}{4}$ - inch slotted test section and exhausts to the atmosphere through a 1.7:1 area-ratio diffuser. The lower wall of the test section was slotted so that 1/5 of the wall area was open. This slotted wall opened into a plenum from which air could be withdrawn by an auxiliary vacuum pump. The tunnel Mach number was varied by increasing tunnel stagnation pressure and/or decreasing the static pressure in the plenum. The Mach number distributions for this test section are discussed in reference 6.

The inlet models were mounted in one face of a spring-mounted cell which was free to flex in the streamwise direction and separated from the tunnel floor by a labyrinth seal. The combined resistance of the flex plate and the force gauges which are attached allowed a maximum deflection of the cell of 0.0015 inch under load. A fouling indicator was provided to insure clearance in the labyrinth seal at all times. Air flow from the inlet and cell was ducted through a flexible hose to a 2-inch exhaust line. A screen was installed at the exit of the settling chamber; downstream of this screen, the air was metered through a calibrated flow nozzle. The system was aspirated by an auxiliary vacuum pump, and a valve in the exhaust line was used to control the mass flow. The stream face of the cell was made small in order to minimize both surface friction drag and interference effects from the tunnel

walls. The width chosen for the cell was 1.8 inches and the model inserts were 1.0 inch wide. Details of the force balance are shown in figure 2.

The inlets tested are shown in figures 3 and 4. The inlet openings ranged from $3/4$ to $3/16$ inch wide and from $3/16$ to $3/4$ inch deep; the width-depth ratio was varied from 4 to $1/4$. The depth is defined as the dimension perpendicular to the inlet center line as shown in figure 3. These inlets range in shape from simple flush inlets of varying inclination and diverging ramp inlets with boundary-layer bypass to scoop inlets of rectangular and circular cross section. Each inlet was followed by a constant-area duct which opened abruptly to the inside of the drag balance cell.

Photographs of the shock patterns in the vicinity of the inlets were made by use of a parallel-beam schlieren system using 6-inch-diameter parabolic mirrors and a mercury arc lamp which had a flash duration of not more than 10 microseconds.

All pressures together with the gross drag were recorded continuously on self-balancing, null-type, electronic-function recorders throughout the Mach number range of the tunnel. Free-stream total pressure and temperature were measured in the upstream duct and the inlet static pressure was measured in the force-balance cell. Other instrumentation included static-pressure orifices in the flow nozzle and a calibrated static-pressure orifice in the tunnel plenum. The inlet mean total pressure \bar{H}_i was calculated from the measured mass-flow rate and the inlet static pressure with the assumption of uniform velocity distribution at the exit of the constant-area duct. These data, for the flush inlets, are restricted to subcritical flow rates due to choking in the calibrated flow nozzle. The test-section Mach number was determined by means of the calibrated plenum static-pressure orifice and the upstream total pressure.

The instrument accuracy of ± 0.2 percent for the electronic recorder provides that the possible error in the computed data shall not be greater than the following:

Quantity	Maximum error for -	
	M = 0.55	M = 1.3
$C_{D,N}$	± 0.03	± 0.005
$C_{D,corr}$	± 0.08	± 0.03
$\frac{\bar{H}_i}{H_\infty}$	± 0.005	± 0.005
$\frac{m_i}{m_\infty}$	± 0.025	± 0.016
M_∞	± 0.0035	± 0.002
$\frac{\Delta p}{q_\infty}$	± 0.04	± 0.009

The Reynolds number of these tests ranged from 3.45×10^6 per foot at a Mach number of 0.55 to 7.0×10^6 per foot at a Mach number of 1.3.

RESULTS AND DISCUSSION

The slotted test section used for this investigation is the same as that used in reference 4. Although the boundary layer at the inlet station was turbulent throughout these tests, both the thickness and profile varied with Mach number. Values of n vary from 5.5 to 8. Boundary-layer thickness varied from 0.15 inch to 0.115 inch at Mach number 0.55 and 1.3, respectively, and was somewhat less than the depth (0.1875 inch) of the basic inlets (width-depth ratio 4).

Schlieren Flow Patterns

Schlieren photographs of the flow in the vicinity of the inlets at Mach numbers 1.0 and 1.3 are presented in figures 5 and 6, respectively. Each row of photographs corresponds to a particular inlet model and directly beneath each photograph the inlet cross section is shown to the scale of the photograph. Inlet mass-flow ratio, also indicated below each photograph, increases from left to right across the page. The small dark spot noted in the photographs near the upstream corner of the inlets (see fig. 5(a), $\theta = 15^\circ$) is caused by a chip in the test-section glass window and does not represent a compression. This dark spot persists throughout all the schlieren photographs presented.

For the flush inlets at $M = 1.0$, these photographs (figs. 5(a) to (d)) are typified by a single shock wave which is generally located at some intermediate position on the ramp for the low-angle inlets but is located near the downstream lip of the higher angle inlets ($\theta \gtrsim 30^\circ$). In addition to the single shock, there exists for many of these inlets a series of curved waves which are usually tangent to the single shock and are more pronounced at low mass-flow rates; at m_i/m_∞ very near zero these waves may lie ahead of the single shock and probably result from disturbances which originated in the inlets and were propagated outward at sonic velocity. Under the influence of the sonic tunnel flow, the disturbances moved downstream at two times the speed of sound but made no progress upstream and therefore became tangent to the single shock. Periodic disturbances of this nature indicate pulsing pressure and a resonance similar to buzz; this was substantiated by the rapid oscillation of the electronic recorders. These recorders, however, were not high-speed-type instruments and therefore neither the frequency nor amplitude of the traces could be relied upon for instantaneous values during pulsing operation. Assuming that these waves traverse the slotted test section laterally at the speed of sound, it is possible to estimate their frequency from their spacing in the schlieren photographs. This is at best a rough approximation since the waves decay rapidly as they are swept downstream and some extrapolation is necessary to determine the spacing at the tops of the waves. By this method it is determined that the frequency is roughly 10,000 to 13,000 cycles per second. This is $2\frac{1}{2}$ times the fundamental frequency of an open ended tube of length equal to the throat length of these auxiliary inlets.

The scoop-inlet flow patterns, figure 5(e), differed from those for the flush inlets in that the pressure field upstream of the inlet caused rather rapid increases in boundary-layer thickness for the low mass-flow rates. Simultaneously, the flow spilled over the inlet lip experiences a supersonic acceleration to a low pressure and then undergoes a normal shock as the flow direction and pressure are reestablished, but the boundary layer becomes separated. As the mass-flow rate is increased, the pressure gradient ahead of the inlet is reduced and the boundary layer becomes thinner, the supersonic expansion and the normal shock weaken, and the extent of flow separation on the downstream fairing is reduced.

At $M = 1.3$, the schlieren photographs (fig. 6), show several shock waves in the flow ahead of the inlets. The furthest upstream wave originates at the labyrinth seal where, because of the subatmospheric tunnel pressure, a small amount of air flows into the tunnel at this Mach number. These disturbances are very weak; the total-pressure loss amounts

to not more than 0.2 percent and the flow almost immediately reestablishes itself at the original Mach number as indicated by the shape of the waves downstream of the labyrinth. The flow disturbance at the plane of the inlet is negligible. At this Mach number the flush inlets again are typified by a single oblique shock wave which generally lies close to the upstream edge of the inlet at low m_i/m_∞ but moves rearward as the inlet mass flow increases. In some cases, for inlets with long ramps, a shock persists near the upstream end of the ramp due to flow separation. It is interesting to note, however, that the flow in the immediate vicinity of the inlet of width-depth ratio 1/4 with fences (see fig. 6(c)) is almost shock free.

The scoop inlets, figure 6(e), are seen to have an additional shock on the fairing downstream of the inlet lips. This shock, which was also observed at $M_\infty = 1.0$, results from reattachment of the flow, following the initial overexpansion of flow spilled from the lips, and forms to reestablish the flow direction parallel to the local surface. A rapidly thickening boundary layer and possible separation occur on the fairing for the circular scoop but are less apparent for the two rectangular scoops.

Some of the waves due to pulsing which were so obvious at $M_\infty = 1.0$ are also present at $M_\infty = 1.3$, although they are masked to a much greater extent by being swept more violently downstream. (See fig. 6(a) for $\theta = 30^\circ$ and 45° and fig. 6(b) for $\theta = 60^\circ$ and 90° .) The frequency appears to be about the same as was noted at $M_\infty = 1.0$.

General Inlet Characteristics

The drag and total-pressure recovery characteristics of the flush inlets are presented in figures 7 to 9, and the characteristics of the scoop inlets are presented in figure 10. In each figure the corrected and net drag coefficients, the inlet static-pressure coefficient, and the total-pressure ratio are presented as functions of the inlet mass-flow ratio for Mach numbers from 0.55 to 1.30. The best index of overall inlet merit is the corrected drag coefficient shown in the upper left-hand corner of each figure. This coefficient represents the net drag less the potential thrust of the inducted air at the end of the constant-area duct. This corrected drag is defined as:

$$C_{D,corr} = C_{D,N} - 2 \frac{m_i}{m_\infty} \sqrt{\frac{1 - \left(\frac{p_\infty}{H_i}\right)^{(\gamma-1)/\gamma}}{1 - \left(\frac{p_\infty}{H_\infty}\right)^{(\gamma-1)/\gamma}}}$$

The net drag coefficient shown in the upper right-hand corner of each figure represents the total momentum of the inducted air plus the losses associated with spillage around the inlet lips. For the flush inlets the variation of $C_{D,N}$ with mass-flow ratio is roughly approximated by

the equation for drag due to a complete loss of momentum, $C_{D,N} = 2 \left(\frac{m_i}{m_\infty} \right)$.

The value of $C_{D,N}$ for the scoop inlets varies widely from this approximation, especially at low flow rates, where the form drag of these inlets is high. This parameter is presented primarily for completeness and will not be further discussed. The inlet static-pressure coefficient shown in the lower left-hand corner provides a direct indication of the internal-pressure level which must be established in order to maintain a given mass-flow rate. In the lower right-hand corner of each figure the pressure available for doing work, or producing a thrust, is shown as the inlet total-pressure ratio. In figure 7(a), it is shown that the corrected drag coefficient of the 15° flush inlet varied between limits of 0 and 0.5. Although these data appear to be random, there is an orderly sequence to the curves as Mach number is increased. Inlet total-pressure ratio (lower right-hand diagram) decreased with Mach number but increased with mass-flow ratio due to the high energy air which is inducted from regions further from the surface as the mass flow is increased. The flat curves of inlet static pressures (lower left) indicate that the mass-flow rate for this inlet is extremely sensitive to small changes in inlet static pressure.

For the 30° , 45° , 60° , and 90° inlets, the corrected drag coefficient increased rapidly with mass-flow ratio, and the curves for the various Mach numbers are better separated and easier to identify than was the case for $\theta = 15^\circ$. The slope of the total-pressure curves decreases steadily as inlet inclination increases (figs. 7(b) to 7(e)) because the internal losses in the system increase at a greater rate than the total pressure of the inducted air. As the slopes of the total-pressure curves decrease, the slopes of the inlet static-pressure curves increase and the system becomes less sensitive to small changes in magnitude of the static pressure.

As the width-depth ratio of the $\theta = 15^\circ$ inlet is reduced from 4 to 1 and to $1/4$, the curves of corrected drag coefficient became somewhat more orderly but overall characteristics were essentially unchanged. (Compare figs. 7(a) and 8.) Fences added to the sides of the inlet of width-depth ratio $1/4$ only served to increase the corrected drag values.

The use of a 7° straight wall or a 7° diverging-wall approach ramp ahead of the 15° inlet led to higher corrected drag coefficients at low mass-flow ratios, especially for Mach numbers near 1.0, and small increases in total-pressure ratios for free-stream Mach numbers greater

than 1.0. (Compare figs. 9(a) and 9(b) with fig. 7(a).) The addition of boundary-layer bypasses to the sides of the diverging-wall ramp resulted in substantial improvements in pressure recovery at the higher mass-flow ratios; these improved total pressures are most apparent in the corrected-drag-coefficient curves which showed a net thrust at a few conditions of low Mach number and high mass flow. This apparent anomaly of a thrust is a result of the finite size of the face of the drag balance cell coupled with a flow from the free-stream boundary layer into the inlet from the sides as well as from the front. This flow into the inlet from the sides demands that the air be turned from its original streamwise direction with accompanying loss of streamwise momentum. This momentum loss does not necessarily require a loss in total pressure. In the present instance, it is believed that part of the air entering from the sides transmits its momentum loss to the surface through shear forces in the boundary layer. Since the face of the drag balance is not wide enough to encompass the full width of the affected flow, the balance readings and values of $C_{D,N}$ will be in error for some conditions of low Mach number and high mass-flow ratios. Values of $C_{D,corr}$ will also be in error for the same conditions. As m_i/m_∞ decreases or as the Mach number increases, these errors become insignificant.

The drag of the scoop configurations, figure 10, was extremely high at low mass-flow ratios but generally decreased with increasing mass flow. The pressure recovery of these configurations was very high because much of the air was taken from the free stream above the boundary layer. It is noted that the two rectangular scoop inlets were probably choked at the higher mass-flow rates. The choke point in each case is apparent in the corrected-drag curves. Total-pressure recovery data beyond choke are not considered reliable.

In order to avoid the complexity of curves of figures 7 to 10, bar graphs of total-pressure ratio and corrected drag coefficients for M_∞ equal to 0.9 and 1.3 have been prepared. These bar graphs are presented as figure 11.

Effects of θ .— The variation of \bar{H}_i/H_∞ and $C_{D,corr}$ with θ for several values of mass-flow ratio is shown in figure 11(a).

For each mass-flow ratio it is observed that \bar{H}_i/H_∞ is a maximum when $\theta = 15^\circ$ and that, for this angle, \bar{H}_i/H_∞ increases with increasing m_i/m_∞ . Decreasing total-pressure recoveries are observed, generally, to accompany increasing values of θ . At $m_i/m_\infty = 0$, the maximum corrected drag coefficient occurred for the $\theta = 15^\circ$ inlet, but at higher mass-flow ratios, the inlets with greater inclinations had the greater drag.

In some instances the inlet total pressure was less than the free-stream static pressure. For these cases, an additional drag which is equivalent to the power needed to compress the air and pump it into the stream has been added to $C_{D,corr}$.

At $M_\infty = 1.3$ (fig. 11(b)), the graphs of total-pressure ratio present a pattern similar to that observed at $M_\infty = 0.9$. Choking in the constant-area duct precluded operation of some of the high θ inlets at the higher mass-flow ratios, especially at $M_\infty = 1.3$.

Effect of width-depth ratio.- An attempt was made to reduce the amount of boundary-layer air entering the inlet by decreasing the width-depth ratio. The results of decreasing width-depth ratio are shown in figures 11(c) and 11(d). At $M_\infty = 0.9$ the variation of total-pressure ratio with width-depth ratio is slight. If the relative proportions of boundary-layer and free-stream air were changed by narrowing the inlets, any increase in total-pressure ratio was almost completely nullified by increased internal losses. Fences added to the sides of the narrowest inlet (width-depth ratio of $1/4$) were ineffective except at the highest mass-flow rates. The drag coefficients for these inlets at equal mass-flow ratios show a definite advantage for the configuration with width-depth ratio of 4. The fences on the inlet width-depth ratio $1/4$ result in increased drag through most of the test range.

At $M_\infty = 1.3$ (fig. 11(d)), the trends of pressure recovery and drag follow those of $M = 0.9$ very closely. The inlets of width-depth ratios 1 and $1/4$ offer better pressure recovery than the wider inlet of width-depth ratio 4; the wide inlet has lower drag for $\frac{m_i}{m_\infty} \leq 0.6$. Fences reduced the drag of the inlet of width-depth ratio $1/4$ at low mass-flow ratio but were particularly detrimental at the higher mass-flow rates for this Mach number.

Effects of ramp configuration, $\phi = 7^\circ$.- Several inlets each having a ramp angle ϕ of 7° and inlet inclination θ of 15° but differing in ramp plan form have been tested, and the results are presented in figures 11(e) and 11(f). The models tested included a rectangular-ramp inlet, a diverging-ramp inlet, and a diverging-ramp inlet which was provided with boundary-layer bleed ramps on both sides of the inlet. These ramps provide a path whereby vortices which form in the corners of the ramp might pass by the inlet. These vortices result from a pressure gradient and attendant cross flow at the edges of diverging-wall ramps, and the scheme of bypassing them is similar to the one reported in reference 7. For $M_\infty = 0.9$ the total-pressure ratio of the rectangular-ramp inlet was lower than that for the diverging-wall ramp inlets, and

the inlet with boundary-layer bypass provided the highest total pressures of any of the flush inlets. At this Mach number, however, the rectangular-ramp inlet provided values of corrected drag coefficient which were less than those of either of the diverging-wall ramp inlets. This appears to be a phenomenon peculiar to the near-sonic range for, at Mach numbers both above and below this range (compare figs. 9(a) and 9(b)), the drag coefficients of the diverging-wall ramp inlet are as low or lower than those of the rectangular-ramp inlet. The boundary-layer-bypass inlet drag coefficient decreases steadily with increasing mass-flow rate and, for $m_1/m_\infty > 0.8$ the drag for this inlet is less than that of any other configuration tested. The inlet velocity ratios of reference 8 are equivalent to the mass-flow ratios of the present paper, and drag characteristics may be compared on this basis. Thus, it is seen that the drag coefficients of reference 8 go to negative values at inlet velocity ratios above about 0.8, whereas the present data show negative drags for mass-flow ratios of 0.52 or greater. Differences in the experimental setups are concerned primarily with the boundary layer in which the inlet operates and with the shape of the inlet lip. The calculations of reference 8 were based entirely upon total-pressure surveys to determine change in momentum, whereas the present paper uses a balance system. In both cases the momentum of the air within the inlet duct is credited to the system as a thrust. Since this correction includes the momentum of the air entering the inlet from the sides as well as from directly upstream, it is obvious that the correction will be excessive; this phenomenon was described earlier in the results where negative corrected drags were found for some flow conditions.

At $M_\infty = 1.3$ (fig. 11(f)), the boundary-layer-bypass inlet again provides the best total-pressure recoveries. The diverging-wall ramp inlet has the lowest drag coefficients at low mass-flow ratios, and the variation of drag coefficient with mass-flow rate at this Mach number is similar to that observed at $M_\infty = 0.9$. At $m_1/m_\infty \lesssim 0.6$ the drag coefficient for the boundary-layer-bypass inlet is less than that for either of the other two 7° ramp inlets.

Effects of scoop inlets.— Bar graphs of the total-pressure and drag-coefficient characteristics of three scoop inlets are presented as figures 11(g) and 11(h). The circular-scoop inlet with a diameter of 0.375 inch extended from the surface out into the stream approximately 2.9 times the boundary-layer thickness at Mach number 1.0. A fairing was provided downstream of the inlet for approximately $5\frac{1}{4}$ inlet diameters. This circular inlet had the highest total-pressure recovery of any of the models tested. The drag coefficients at low mass-flow rates, however, are higher than those for any other inlet at both $M_\infty = 0.9$ and $M_\infty = 1.3$ but decrease rapidly with increasing mass-flow rate.

The two rectangular scoop inlets are $3/4$ inch wide and $3/16$ inch high. One has an axial inclination θ of 15° and the other, 90° ; both had downstream fairings which were 12 inlet heights in length. These inlets were formed from the corresponding flush inlets by adding the scoop and downstream fairing. Consequently, for the $\theta = 90^\circ$ inlet, l/d was increased to 5.63 and for the $\theta = 15^\circ$ inlet, l/d was increased to 6.78. Based on the results of reference 4, this range of l/d should have little if any effect on inlet performance. Therefore, it must be concluded that any variation in performance between the two rectangular scoop inlets is a result of differences in internal flow due to differences in θ . At $M_\infty = 0.9$ the 15° scoop had slightly better pressure recovery than the 90° inlet and at $M_\infty = 1.3$ the pressure recoveries were very nearly equal for these two inlets.

At $M_\infty = 0.9$ the scoop inlet for $\theta = 90^\circ$ provided lower drag than the scoop inlet for $\theta = 15^\circ$ at all except the highest mass-flow ratios. At $M_\infty = 1.3$ the drag coefficients were very nearly equal. It must be noted that in all cases the larger circular-scoop inlet provided higher total-pressure recoveries but also produced higher drag coefficients than either of the rectangular scoops which extended from the surface only slightly beyond the edge of the boundary layer.

Minimum-Drag Design Data

For each inlet the minimum value of $C_{D,corr}$ per unit of mass flow has been obtained by passing a line through the origin and swinging it upward until it touches the $C_{D,corr}$ curve. Normally, the line from the origin would be tangent to the $C_{D,corr}$ curve. Many of these inlets, however, could provide two tangent points, one having a greater slope than the other, if the inlet static pressure had been carried below the point where choking occurs. In many cases the tangent point at choke conditions would be the one corresponding to the lowest drag per unit mass flow. In such cases, the last data point available has been used as a tangent since these points closely approximate choke mass flow. The corresponding mass-flow ratio was then used to determine the inlet area which would be required so that the actual mass flow into the inlet would be the same as that in a free-stream tube of an arbitrary area, A_∞ . This provides a comparison of the inlet area required when each of the various inlets operates at the same absolute mass flow, but the mass-flow ratio corresponds to the minimum drag point. The areas thus found divided by the basic free-stream tube area A_∞ have been plotted as a function of Mach number in figure 12. It is noted that these data are merely the reciprocals of the mass-flow ratios for minimum drag.

For these curves it is observed that a high-total-pressure-recovery inlet requires only a small inlet area; whereas, flush rectangular inlets of $\theta = 60^\circ$ and $\theta = 90^\circ$ were very large.

A comparison of minimum drag for these various inlets may be obtained (for equal mass flow) if the original value of $C_{D,corr}$ is multiplied by A/A_∞ . This comparison places each inlet on an equal basis by using a common reference area. It is seen that the $\theta = 15^\circ$ inlet has a much lower drag than the inlets where $\theta > 15^\circ$. (See fig. 13(a).)

For the inlet series varying in width-depth ratio (fig. 13(b)), it is seen that width-depth ratio 1/4 is desirable for $M > 0.9$ but that for $M < 0.9$ a width-depth ratio of 1 or 4 inlet is better. The inlet with fences had comparatively high drags throughout the test Mach number range.

The inlet with boundary-layer bypass was the best of the 7° ramp series. (See fig. 13(c).) Drags for the diverging-ramp inlet were surprisingly high for $0.8 < M < 1.3$. Note that these data have been refaired to $C_{D,corr}$ equal to zero for those conditions which indicated thrust in figure 9.

For the rectangular-scoop inlets (fig. 13(d)), the differences between the 15° and 90° inlets were slight, whereas the circular-scoop-inlet drag was much higher for $M < 1.2$, above this Mach number the circular scoop was superior.

In general, the inlet with boundary-layer bypass had the lowest drag of all inlets tested for all Mach numbers except 1.3 where the circular-scoop inlet was best. It must be emphasized, however, that this result is based on operation at the mass-flow ratio corresponding to minimum $C_{D,corr}$. The variation of $C_{D,corr}$ with mass-flow ratio is such that operation at any other mass-flow ratio may result in large increases in drag.

CONCLUSIONS

An experimental investigation of the total-pressure recovery and drag characteristics of several auxiliary air inlets which had dimensions comparable with those of the thickness of the boundary layer has yielded the following conclusions which are based on equal mass-flow rates for these inlets when each is operated at its minimum-drag mass-flow ratio.

1. In a series of rectangular flush inlets wherein the inlet inclination angle varied from 15° to 90° , the lowest drag and highest total-pressure recovery for any given flow rate was always attained with the inlet of lowest inclination.

2. A rectangular flush inlet with axial inclination of 15° and width-depth ratio of $1/4$ had lower transonic drag coefficients than an inlet with a width-depth ratio of 1 or 4. At Mach numbers less than 0.9, the inlets with width-depth ratio ≥ 1.0 had lower drag.

3. A boundary-layer bypass at the sides of a diverging-ramp inlet produced the highest total-pressure recoveries of any of the flush inlets tested and the lowest drag of any of the test inlets for the range of Mach numbers from 0.55 to 1.2.

4. The circular-scoop inlet had the highest total-pressure recovery of any of the inlets tested; the drag coefficient for this inlet was low at Mach number 1.3 but was very high for all other Mach numbers tested.

5. Low drag for high-recovery inlets generally occurred at or near maximum mass-flow ratios.

6. Multiple shock waves which arise from a pulsating or resonant phenomenon similar to that observed in buzz were observed near the entrance of many of these inlets, especially at Mach numbers near 1.0 and at low mass-flow ratios.

Langley Research Center,
National Aeronautics and Space Administration,
Langley Field, Va., August 27, 1958.

REFERENCES

1. Rogallo, F. M.: Internal-Flow Systems for Aircraft. NACA Rep. 713, 1941.
2. Simon, Paul C.: Internal Performance of a Series of Circular Auxiliary-Air Inlets Immersed in a Turbulent Boundary Layer Mach Number Range: 1.5 to 2.0. NACA RM E54103, 1955.
3. Huff, Ronald G., and Anderson, Arthur R.: Internal Performance of Several Auxiliary Air Inlets Immersed in a Turbulent Boundary Layer at Mach Numbers of 1.3, 1.5, and 2.0. NACA RM E56J18, 1957.
4. Dennard, John S.: A Transonic Investigation of the Mass-Flow and Pressure Recovery Characteristics of Several Types of Auxiliary Air Inlets. NACA RM L57B07, 1957.
5. Simon, Paul C., and Kowalski, Kenneth L.: Charts of Boundary-Layer Mass Flow and Momentum for Inlet Performance Analysis - Mach Number Range, 0.2 to 5.0. NACA TN 3583, 1955.
6. Nelson, William J., and Cabbage, James M., Jr.: Effects of Slot Size and Geometry on the Flow in Rectangular Tunnels at Mach Numbers up to 1.4. NACA RM L53B16, 1953.
7. Taylor, Robert A.: Some Effects of Side-wall Modifications on the Drag and Pressure Recovery of an NACA Submerged Inlet at Transonic Speeds. NACA RM A51103a, 1952.
8. Mossman, Emmet A., and Randall, Lauros M.: An Experimental Investigation of the Design Variables for NACA Submerged Duct Entrances. NACA RM A7I30, 1948.

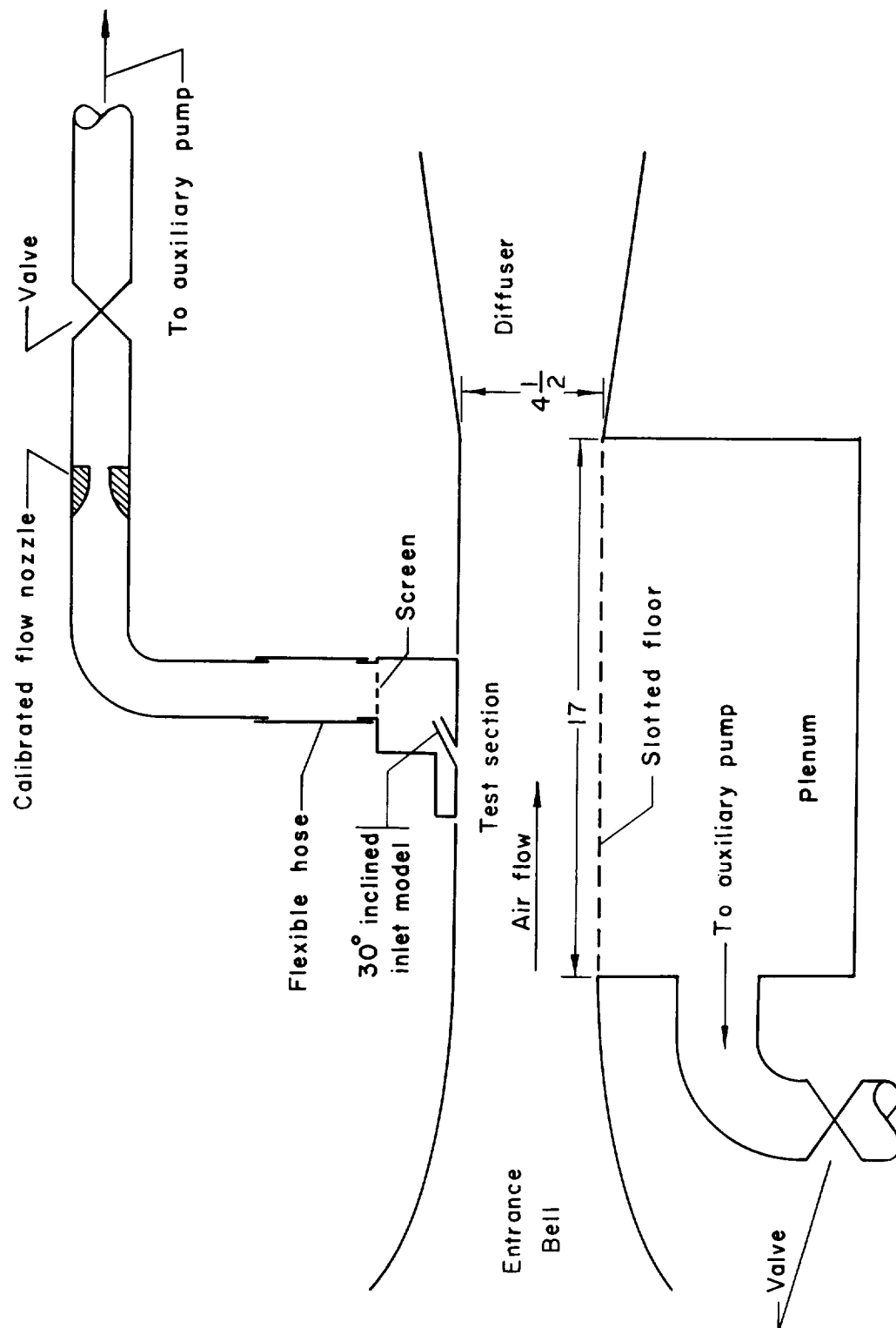


Figure 1.- Line drawing showing the general arrangement of the flow system. Linear dimensions are in inches.

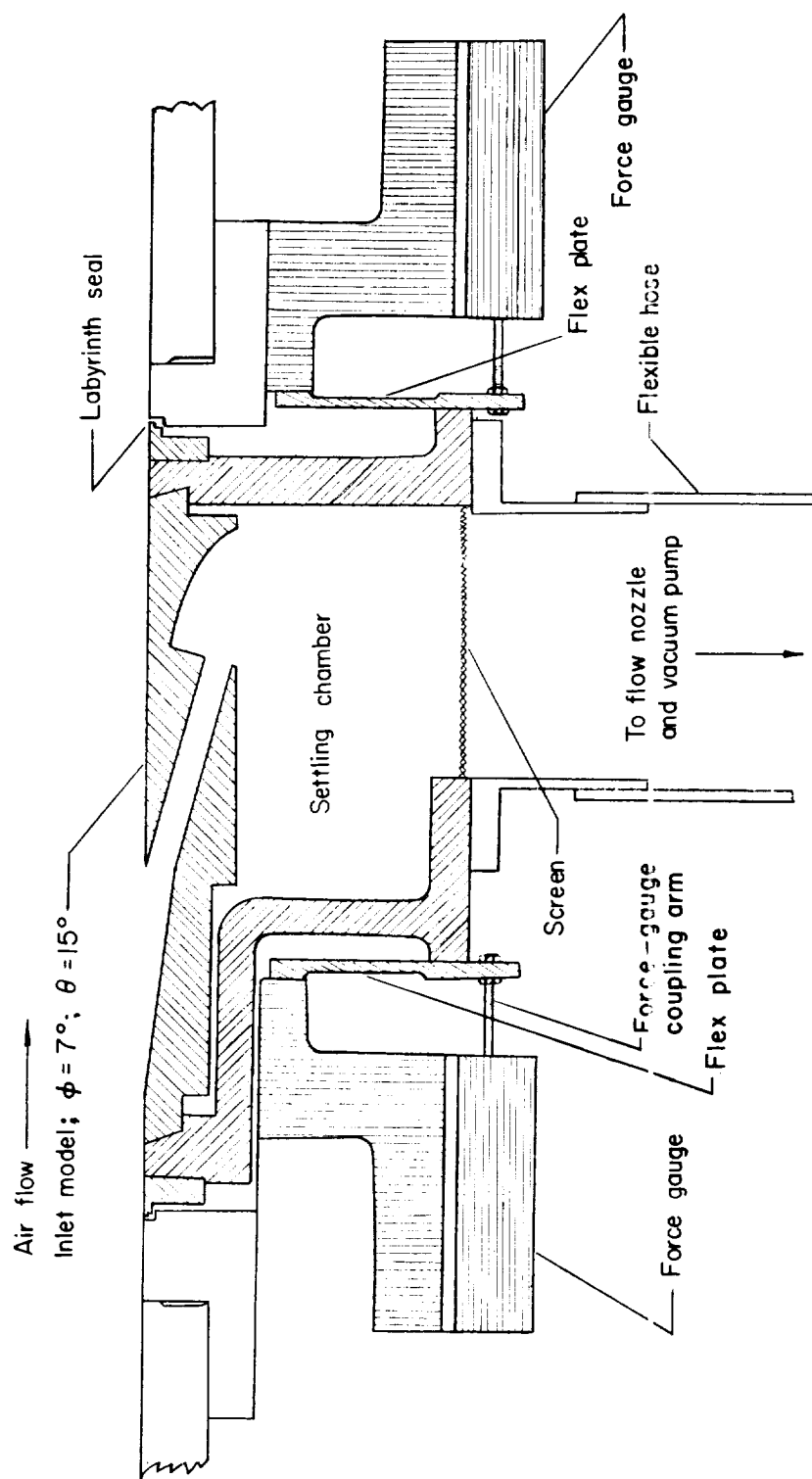
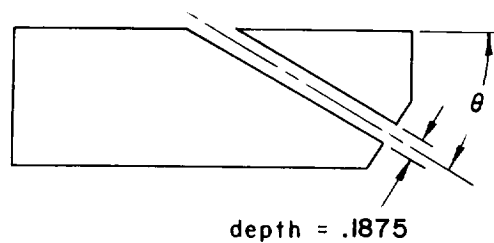


Figure 2.- Details of the inlet-model installation in the force balance.

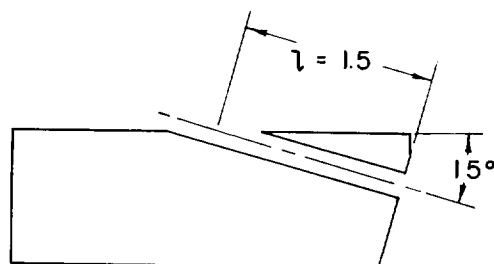


Inclined rectangular inlets
width-depth ratio = 4

$$l/d = 5$$

Variable:

$$\theta = 15^\circ, 30^\circ, 45^\circ, 60^\circ, 90^\circ$$



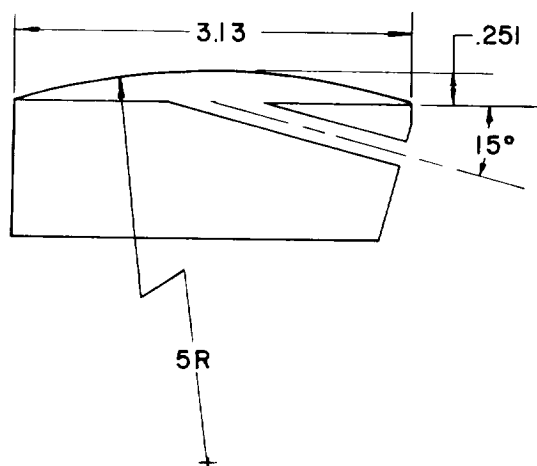
Rectangular inlets

$$\theta = 15^\circ$$

$$l/d = 5$$

Variable:

width-depth ratio = 4, 1, 1/4



Rectangular inlet

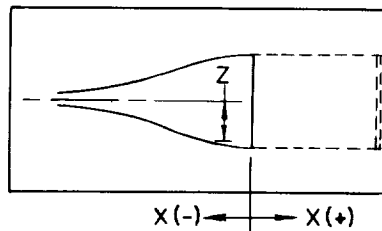
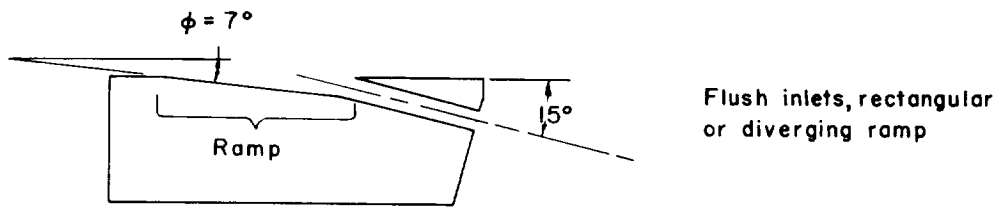
width-depth ratio = 1/4
with boundary layer fences

$$l/d = 5$$

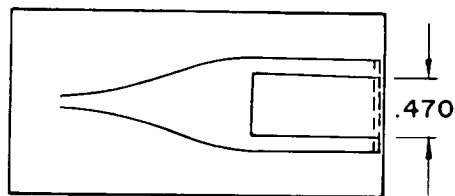
$$\theta = 15^\circ$$

(a) Flush rectangular inlets.

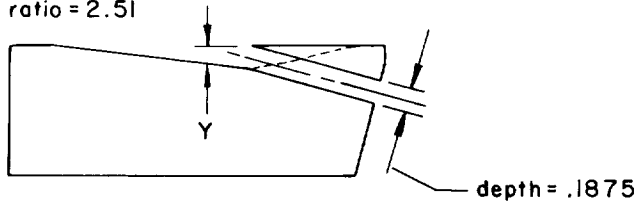
Figure 3.- Line drawings of the inlets tested. All linear dimensions are in inches.



Top view: flush rectangular inlet with diverging ramp



Top view: flush rectangular inlet with diverging ramp and boundary-layer-bypass ramps; width-depth ratio = 2.51

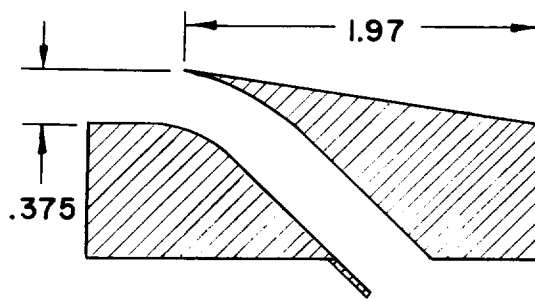


Side view: boundary-layer-bypass inlet.

Ramp Coordinates		
X	Y	Z
-1.50	0	0.032
-1.35		.060
-1.20		.088
-1.05		.118
-.90		.146
-.75	Straight ramp 7°	.175
-.60		.230
-.45		.287
-.30		.339
-.15		.373
0	0.181	.375
0.125	.173	
.250	.154	
.375	.124	
.500	.090	
.625	.056	
.750	.026	
.875	.007	
1.000	0	

(b) Ramp inlet, $\phi = 7^\circ$.

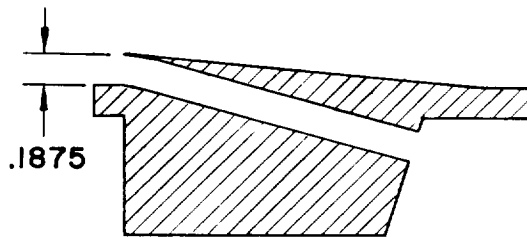
Figure 3.- Continued.



Circular-scoop inlet

$$l/d = 6.8$$

$$\theta = 45^\circ$$

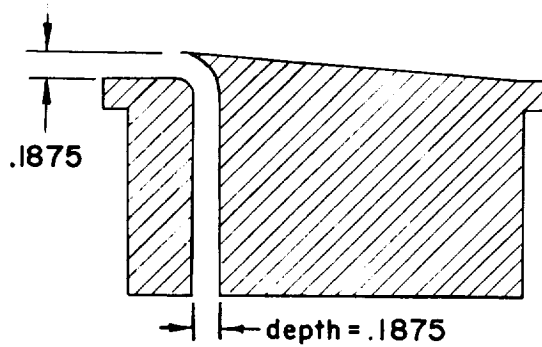


Rectangular-scoop inlet

width-depth ratio = 4

$$l/d = 6.78$$

$$\theta = 15^\circ$$



Rectangular-scoop inlet

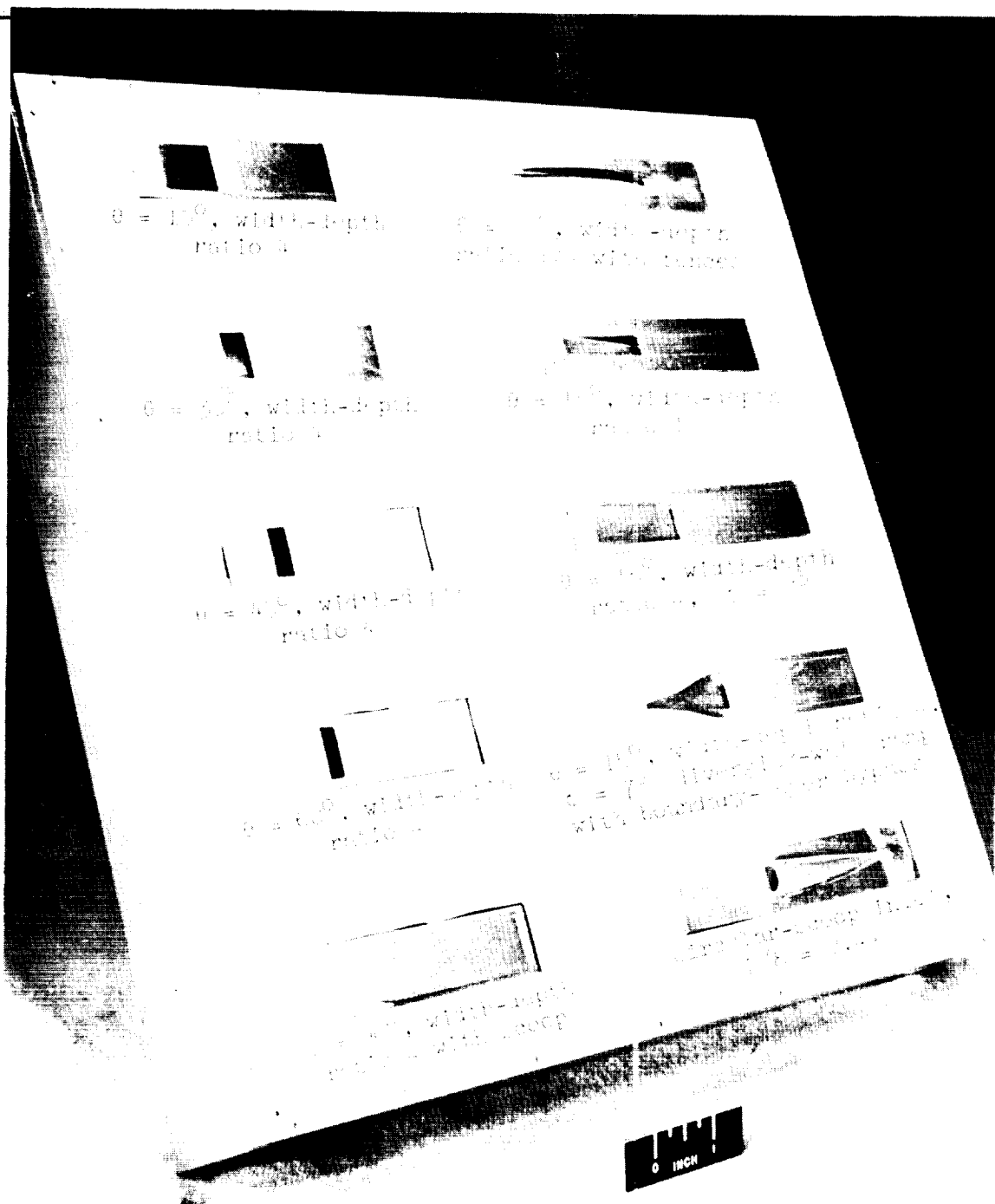
width-depth ratio = 4

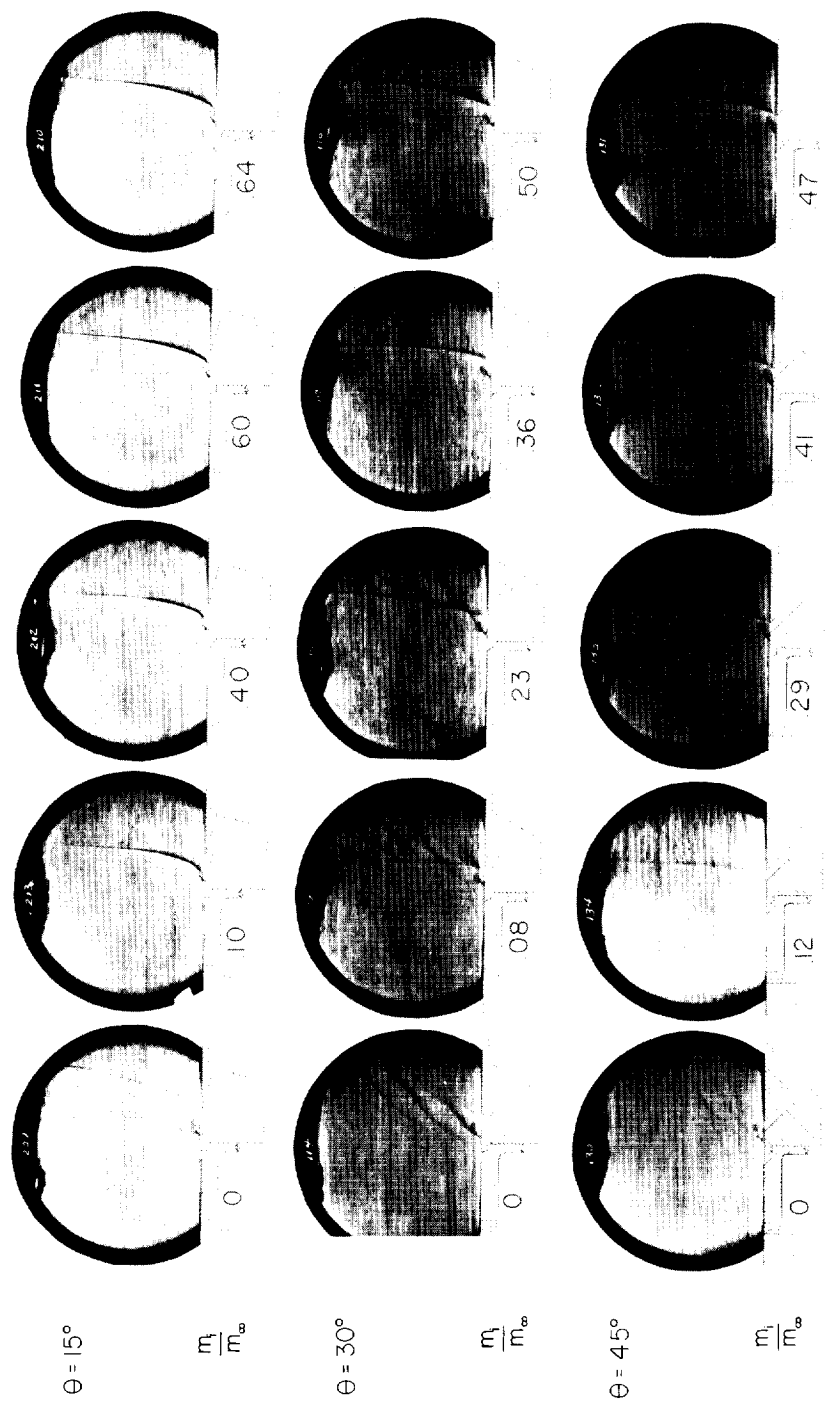
$$l/d = 5.63$$

$$\theta = 90^\circ$$

(c) Scoop inlets.

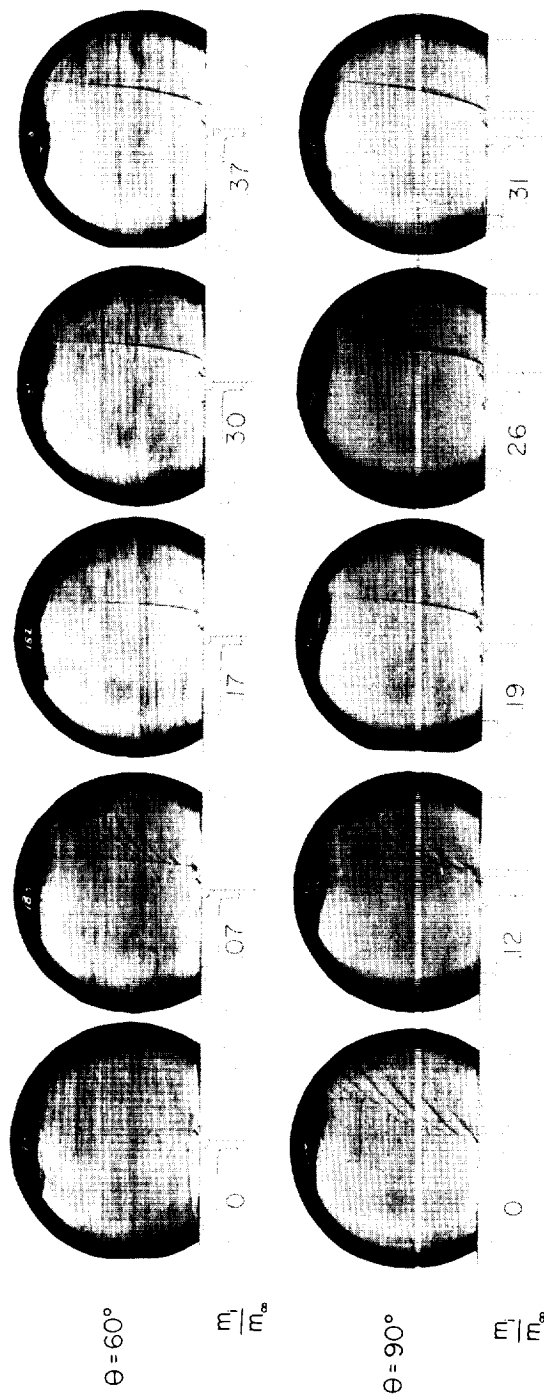
Figure 3.- Concluded.





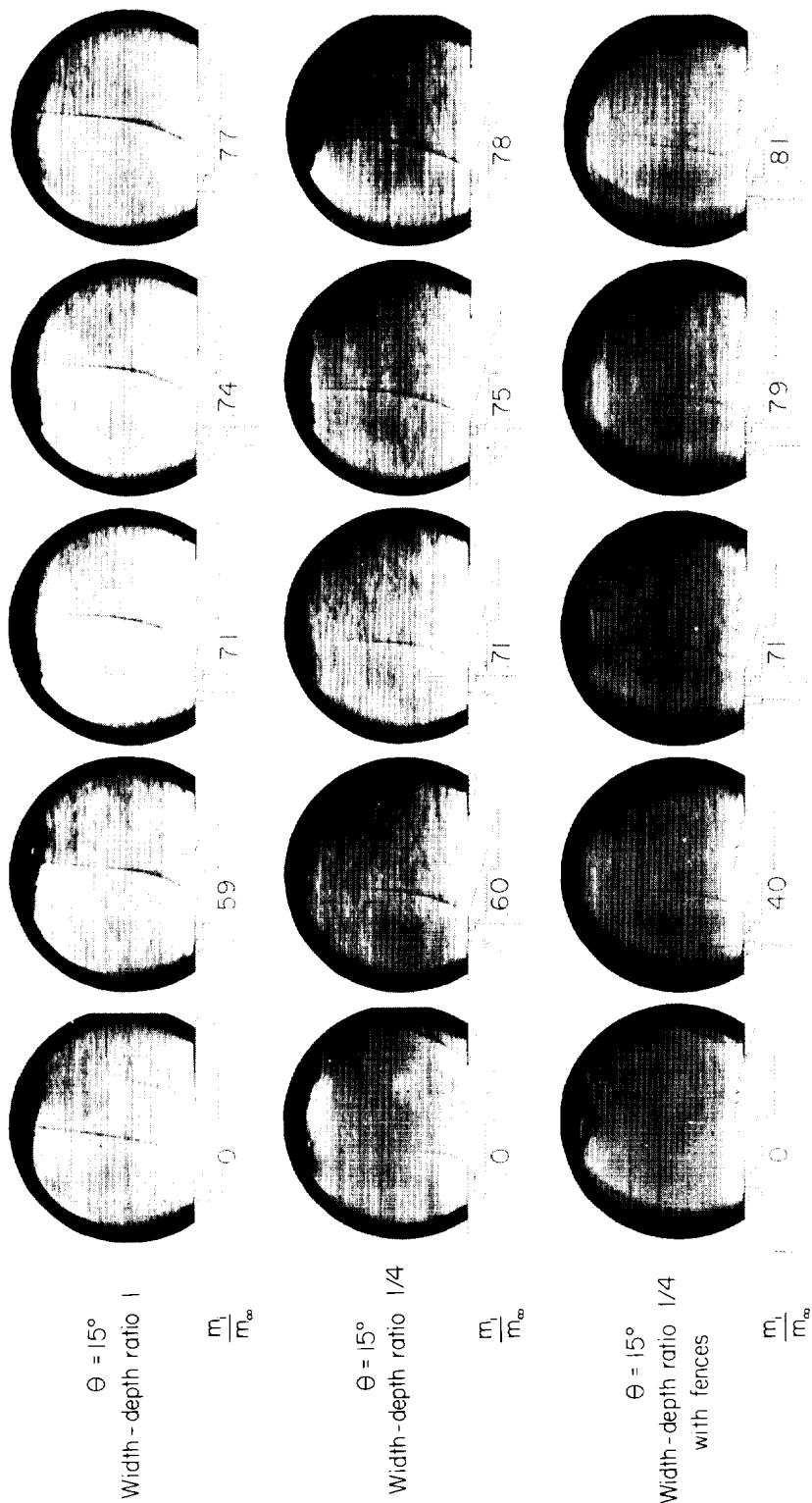
(a) Flush rectangular inlets; $l/d = 5$; width-depth ratio, 4; $\theta = 15^\circ, 30^\circ, 45^\circ$. L-58-2542

Figure 5.- Schlieren photographs of inlet models. $M = 1.0$.



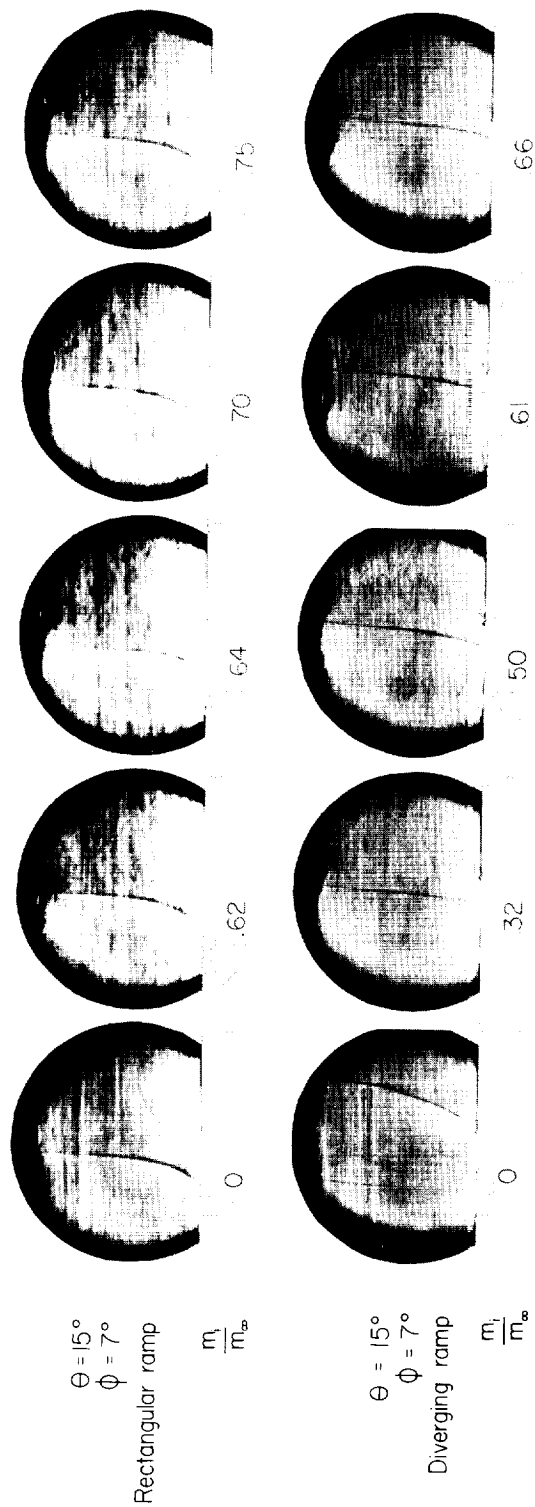
(b) Flush rectangular inlets; $l/d = 5$; width-depth ratio, 4; $\theta = 60^\circ, 90^\circ$. L-58-2543

Figure 5.- Continued.



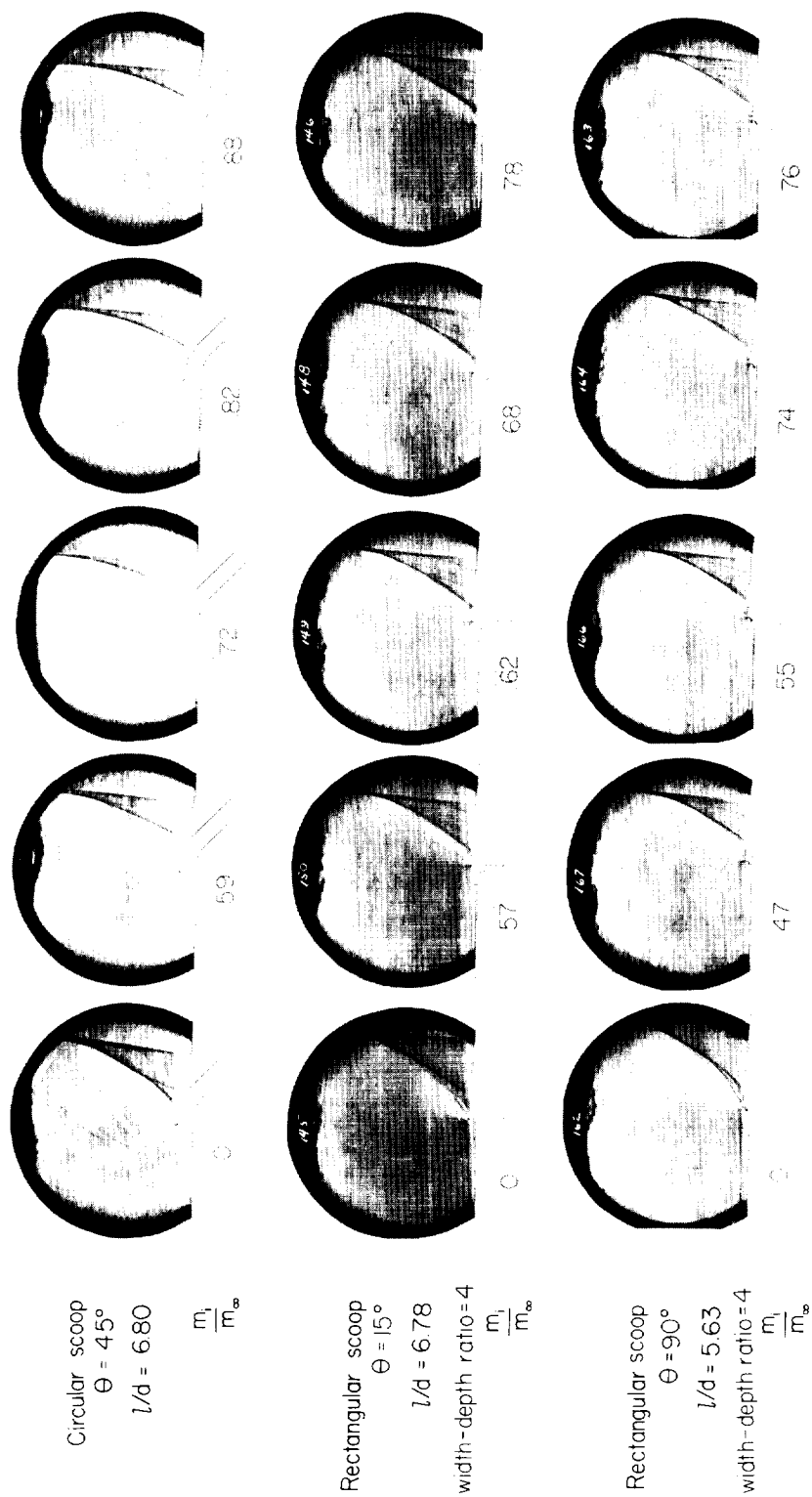
(c) Flush rectangular inlets; width-depth ratio, 1 and 1/4; $\nu/d = 5$; $\theta = 15^\circ$. L-58-2544

Figure 5.- Continued.



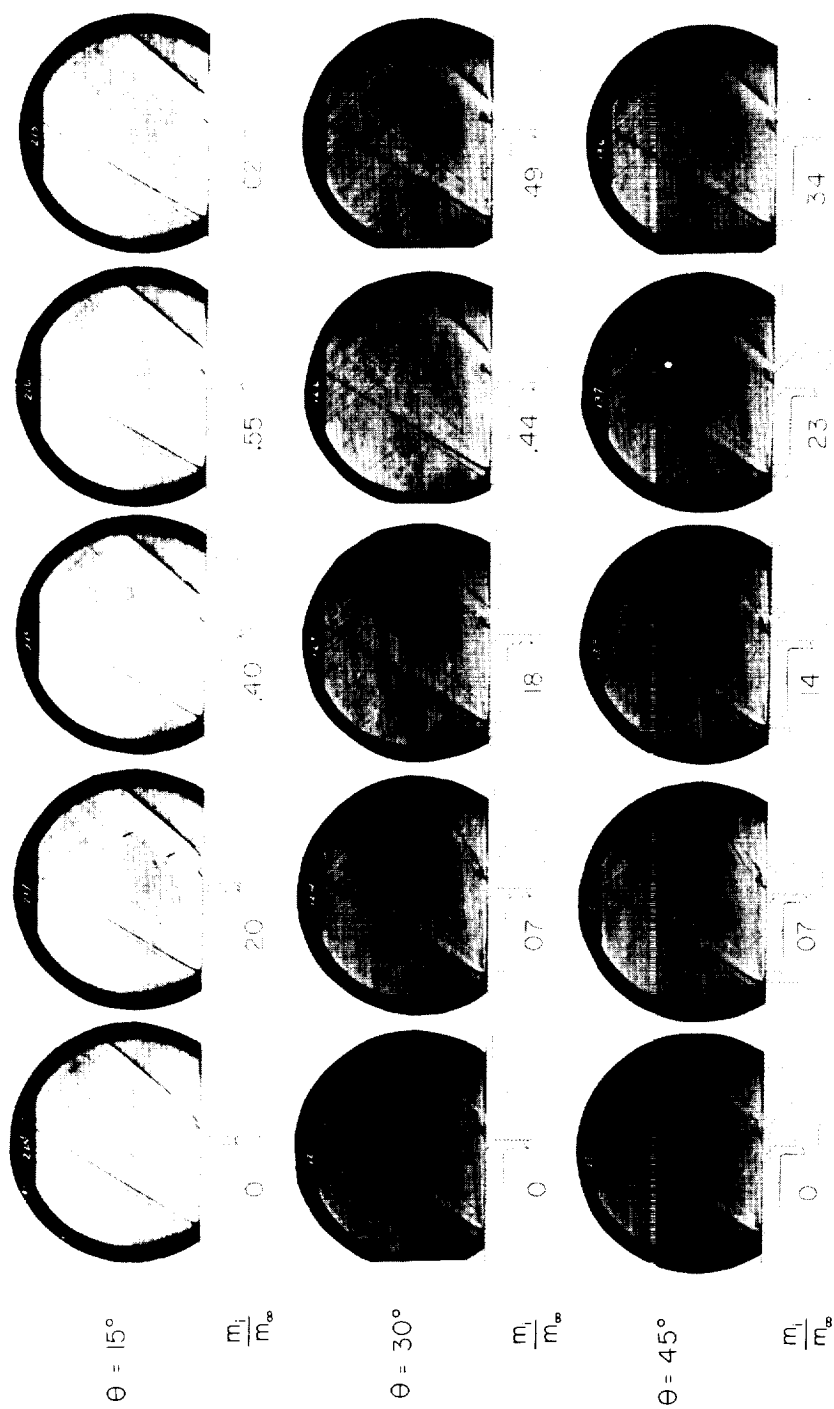
(d) Flush rectangular inlets; width-depth ratio, 4; $l/d = 5$; $\theta = 15^\circ$; $\phi = 7^\circ$. L-58-2545

Figure 5.- Continued.



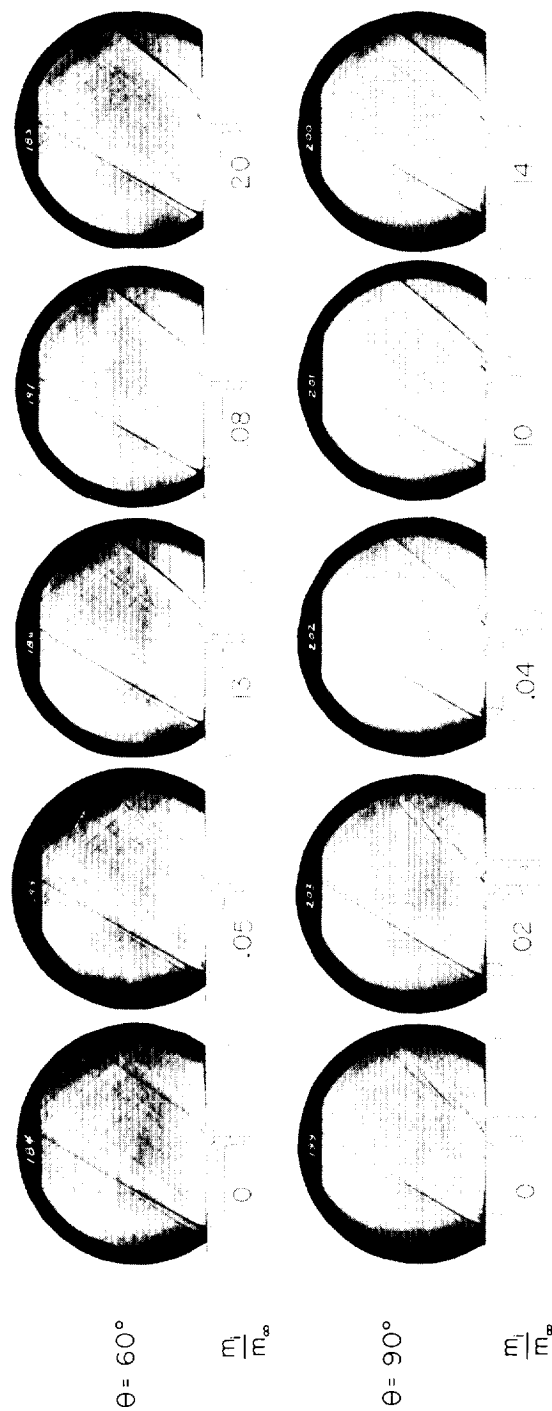
(e) Scoop inlets; $l/d = 6.80, 6.78, 5.63$; $\theta = 45^\circ, 15^\circ, 90^\circ$. L-58-2546

Figure 5.- Concluded.

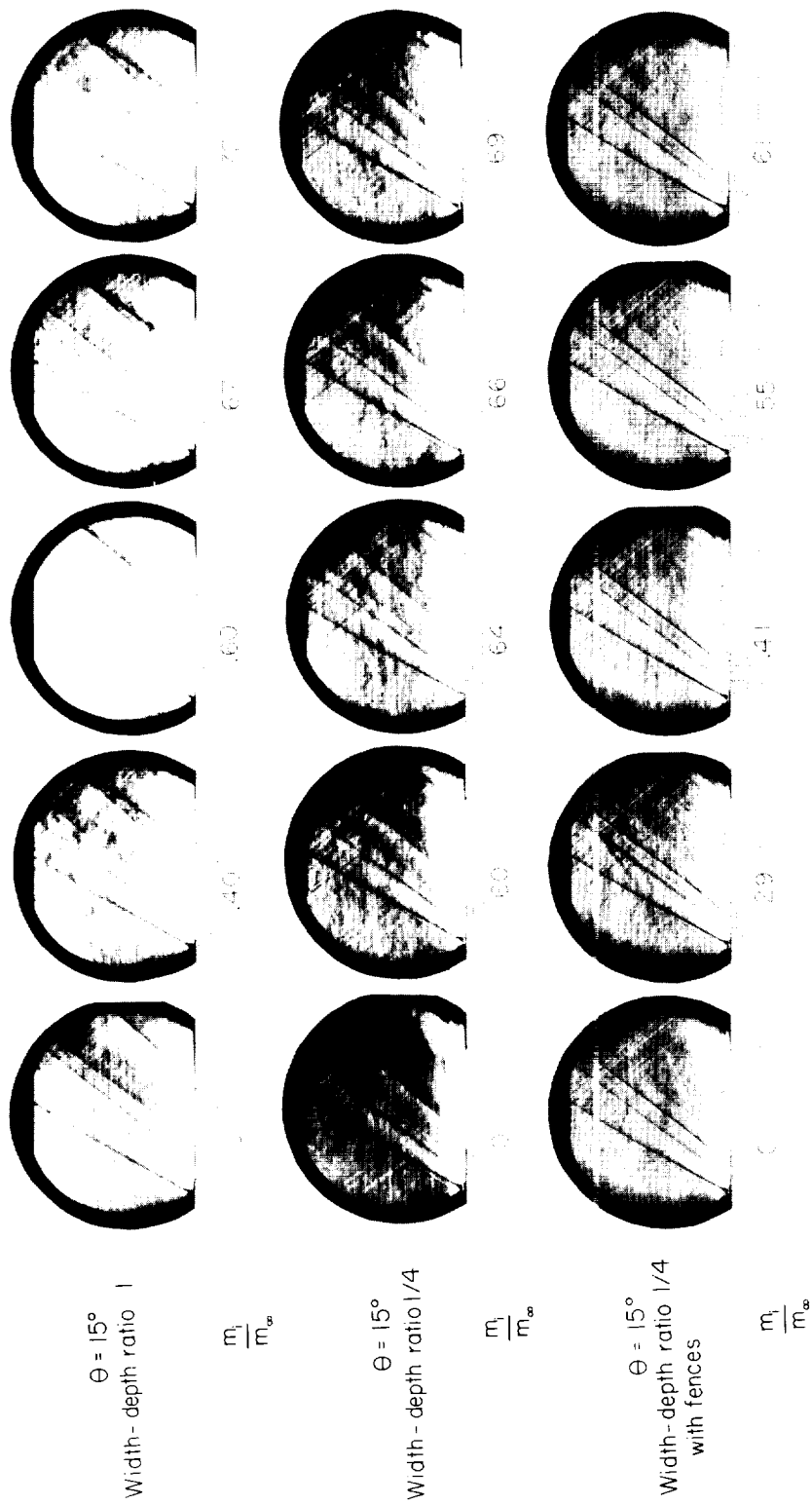


(a) Flush rectangular inlets; $l/d = 5$; width-depth ratio, 4; $\theta = 15^\circ, 30^\circ, 45^\circ$. L-58-2547

Figure 6.- Schlieren photographs of inlet models. $M = 1.3$.

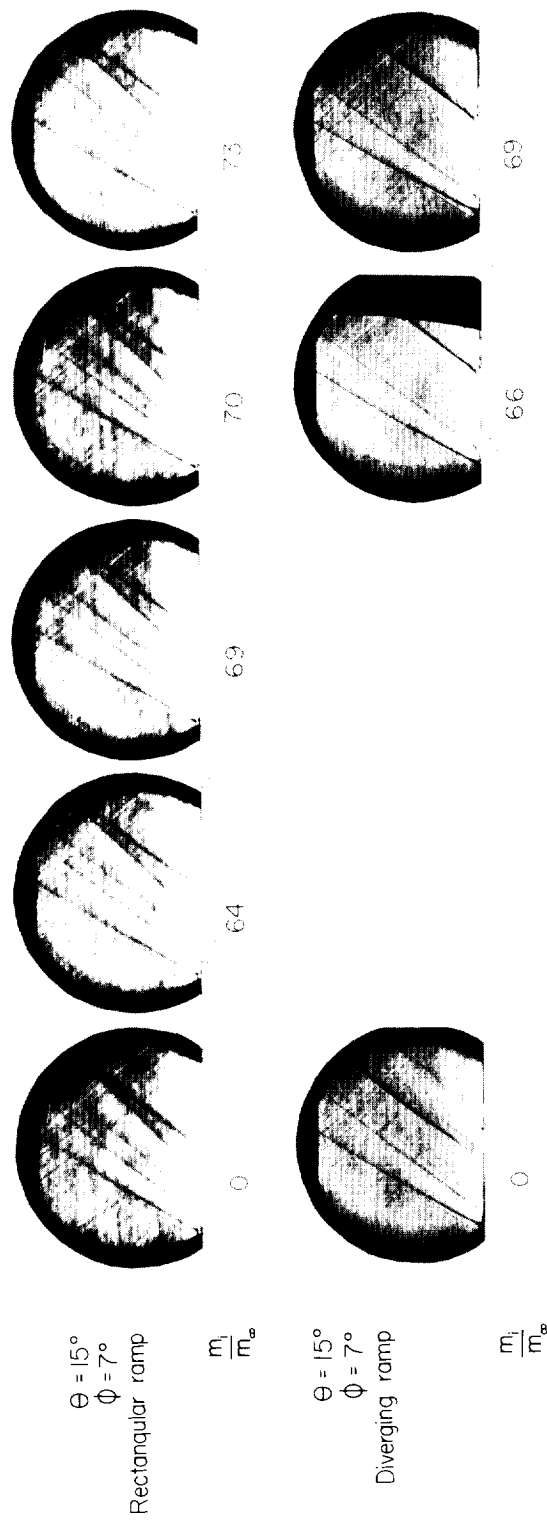


(b) Flush rectangular inlets; $\lambda/d = 5$; width-depth ratio, 4; $\theta = 60^\circ, 90^\circ$. L-58-2548
Figure 6.- Continued.



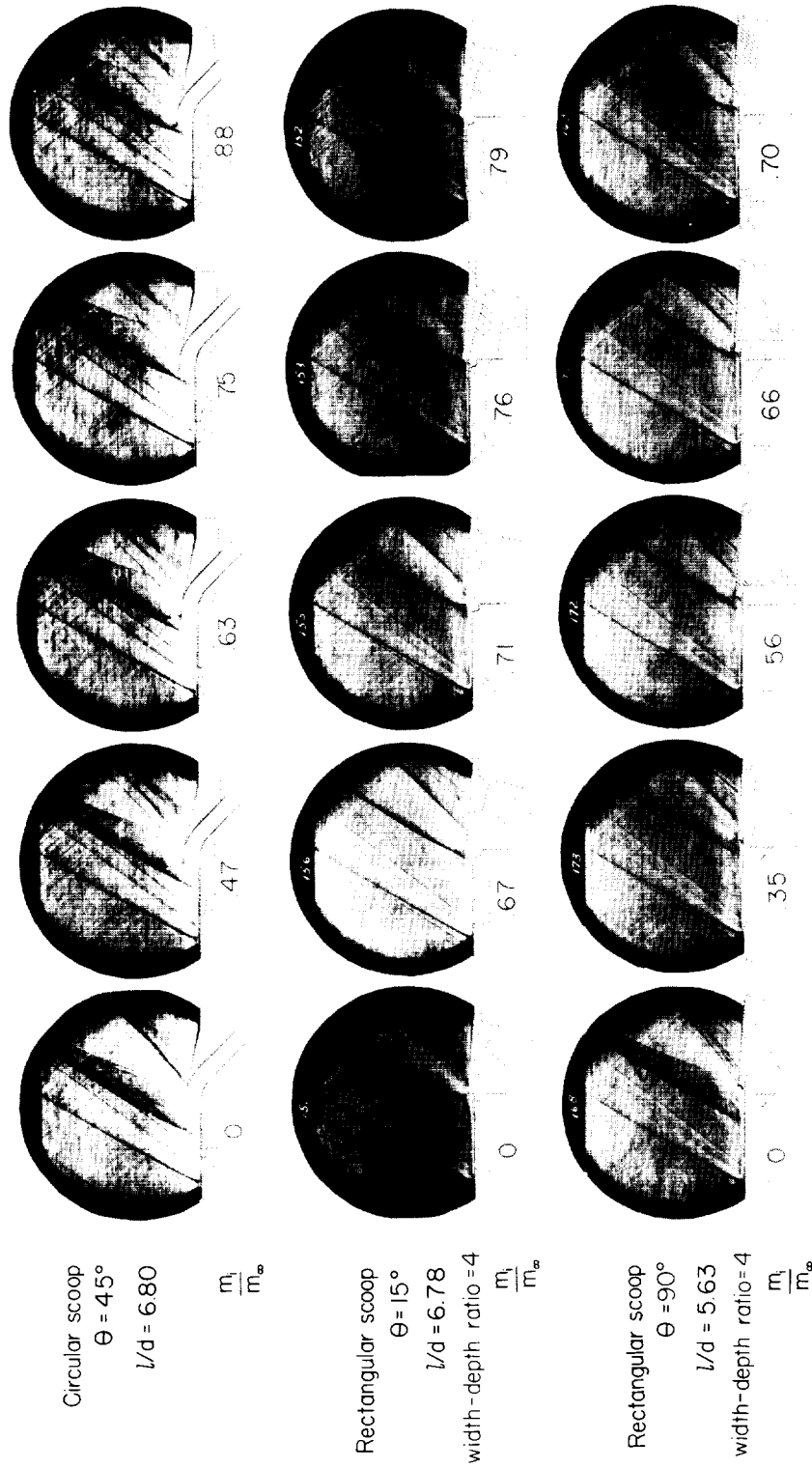
(c) Flush rectangular inlets; width-depth ratio, 1 and 1/4; $\ell/d = 5$; $\theta = 15^\circ$. L-58-2549

Figure 6.- Continued.



(d) Flush rectangular inlets; width-depth ratio, 4; $l/d = 5$; $\theta = 15^\circ$; $\phi = 7^\circ$. I-58-2550

Figure 6.- Continued.



(e) Scoop inlets; $l/d = 6.80, 6.78, 5.63$; $\theta = 45^\circ, 15^\circ, 90^\circ$. L-58-2551

Figure 6.- Concluded.

12-21-58L

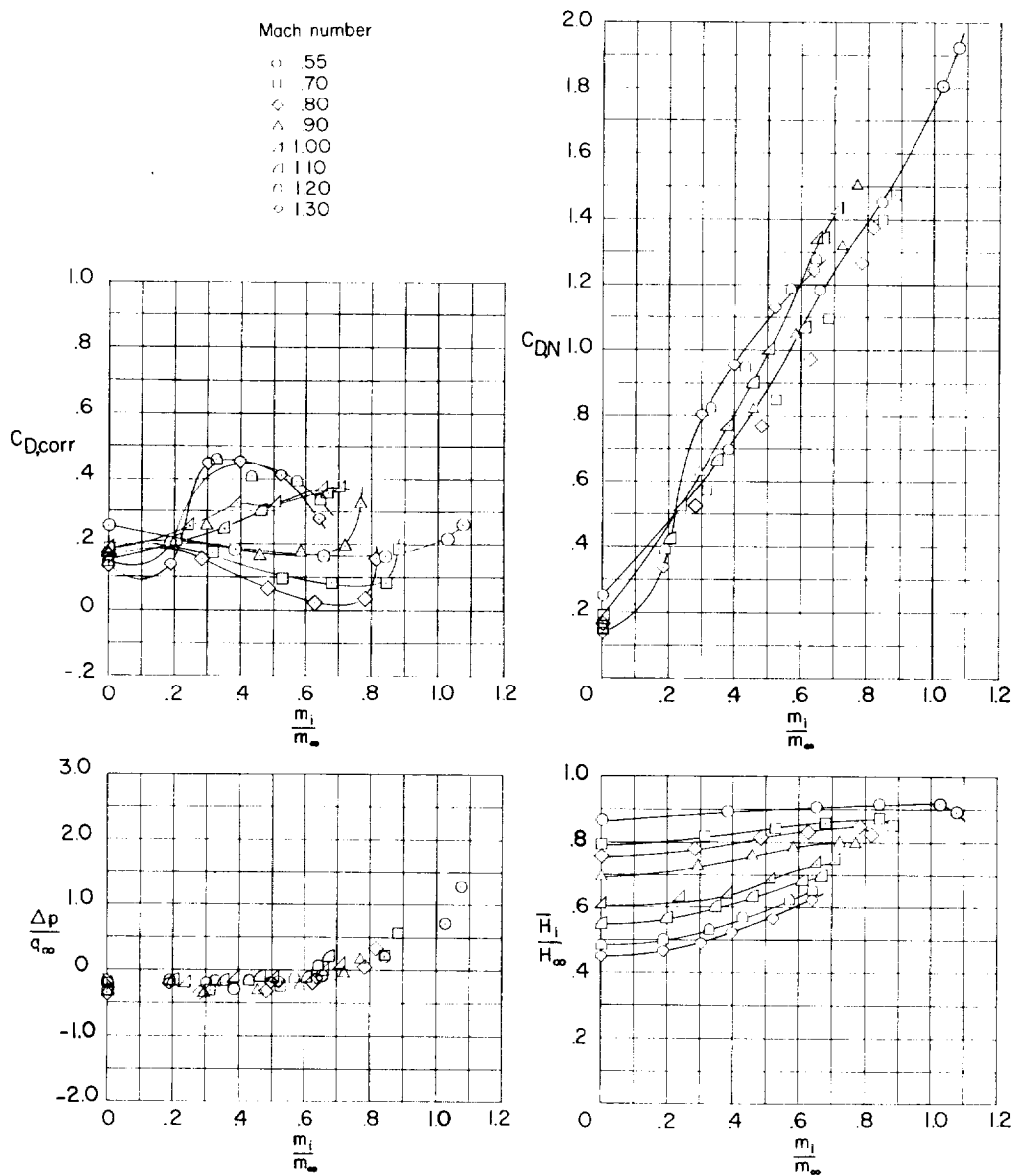
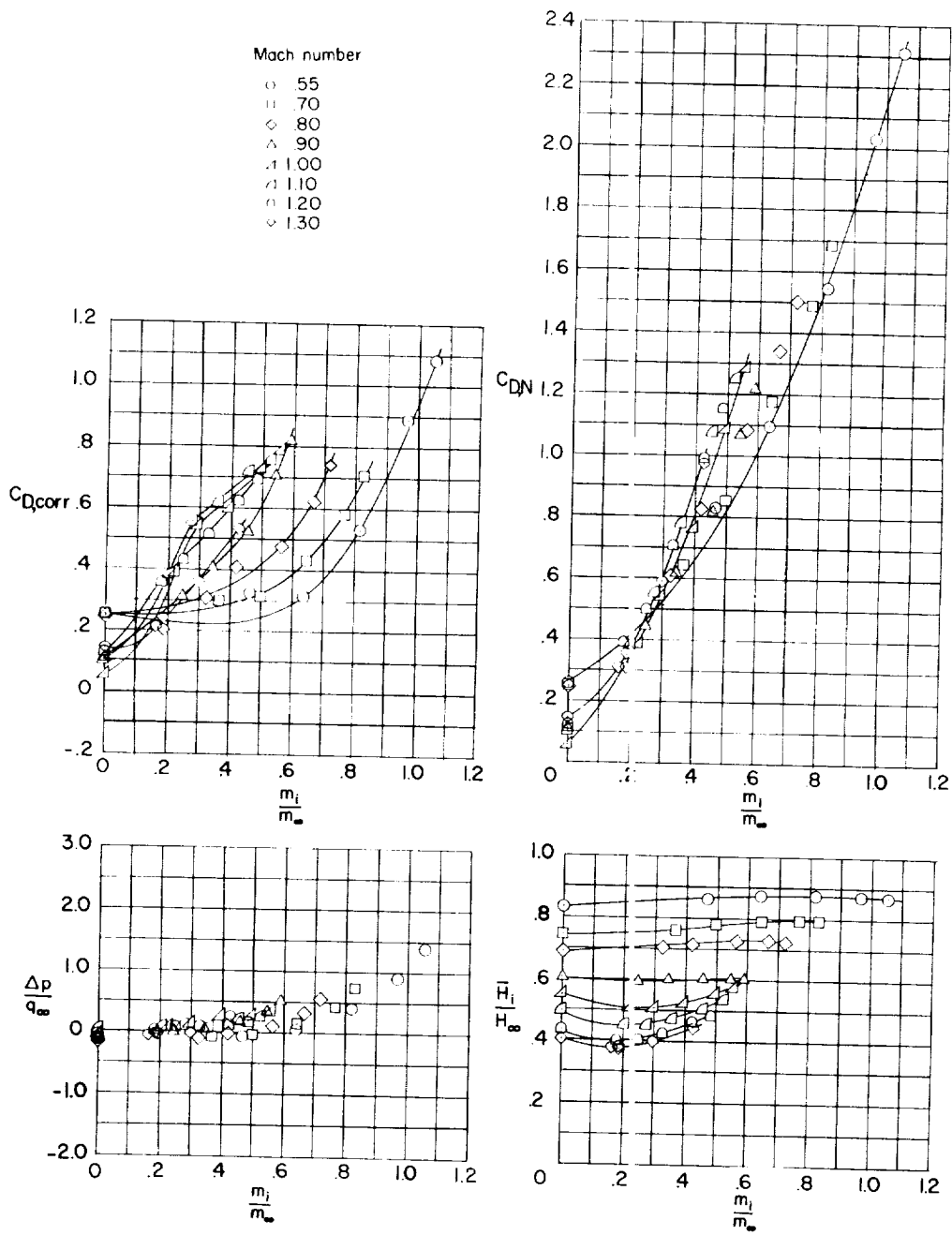
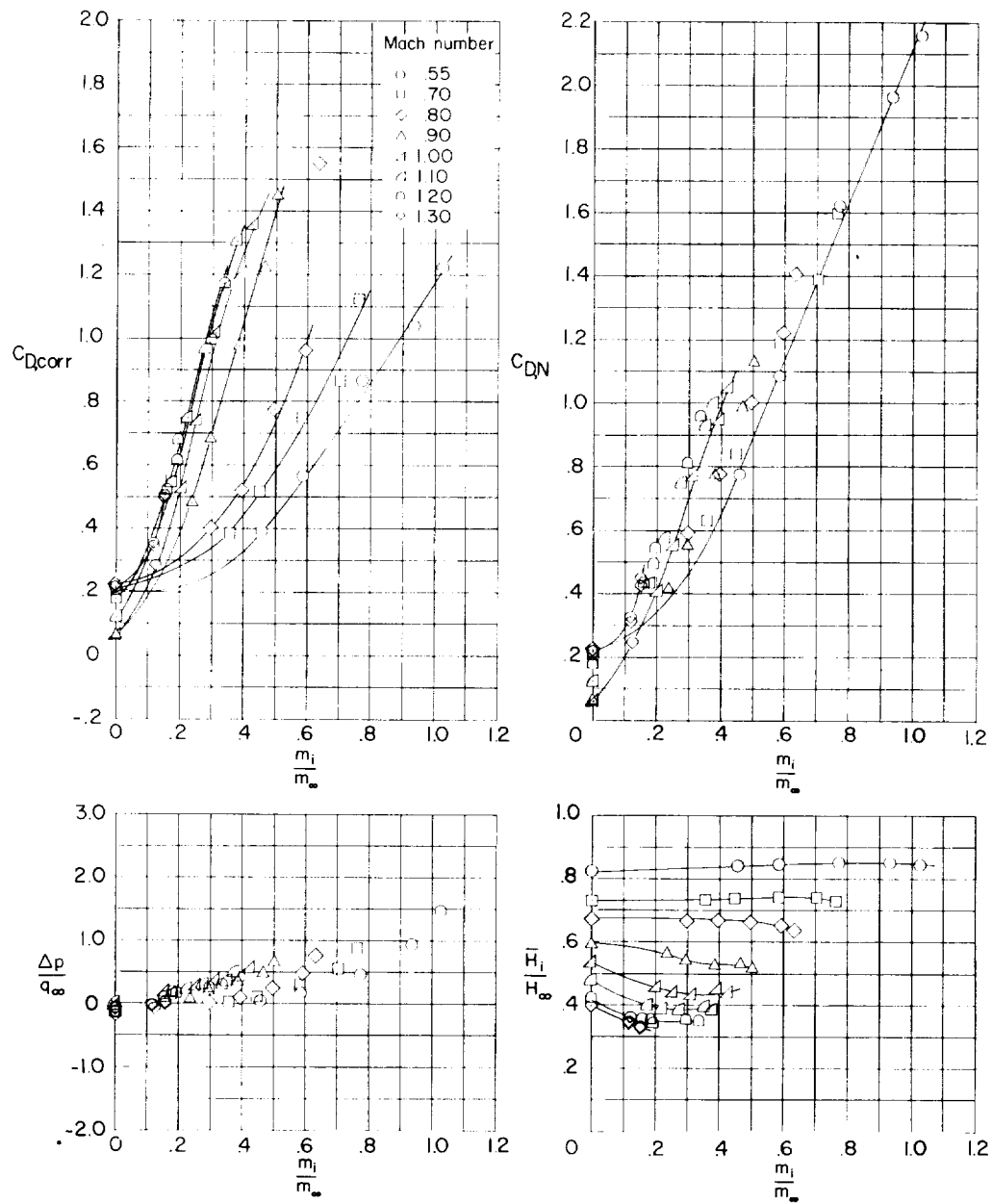
(a) $\theta = 15^\circ$.

Figure 7.- Drag and pressure recovery characteristics of flush rectangular inlets of varying inclination. Width-depth ratio, 4; $l/d = 5$.



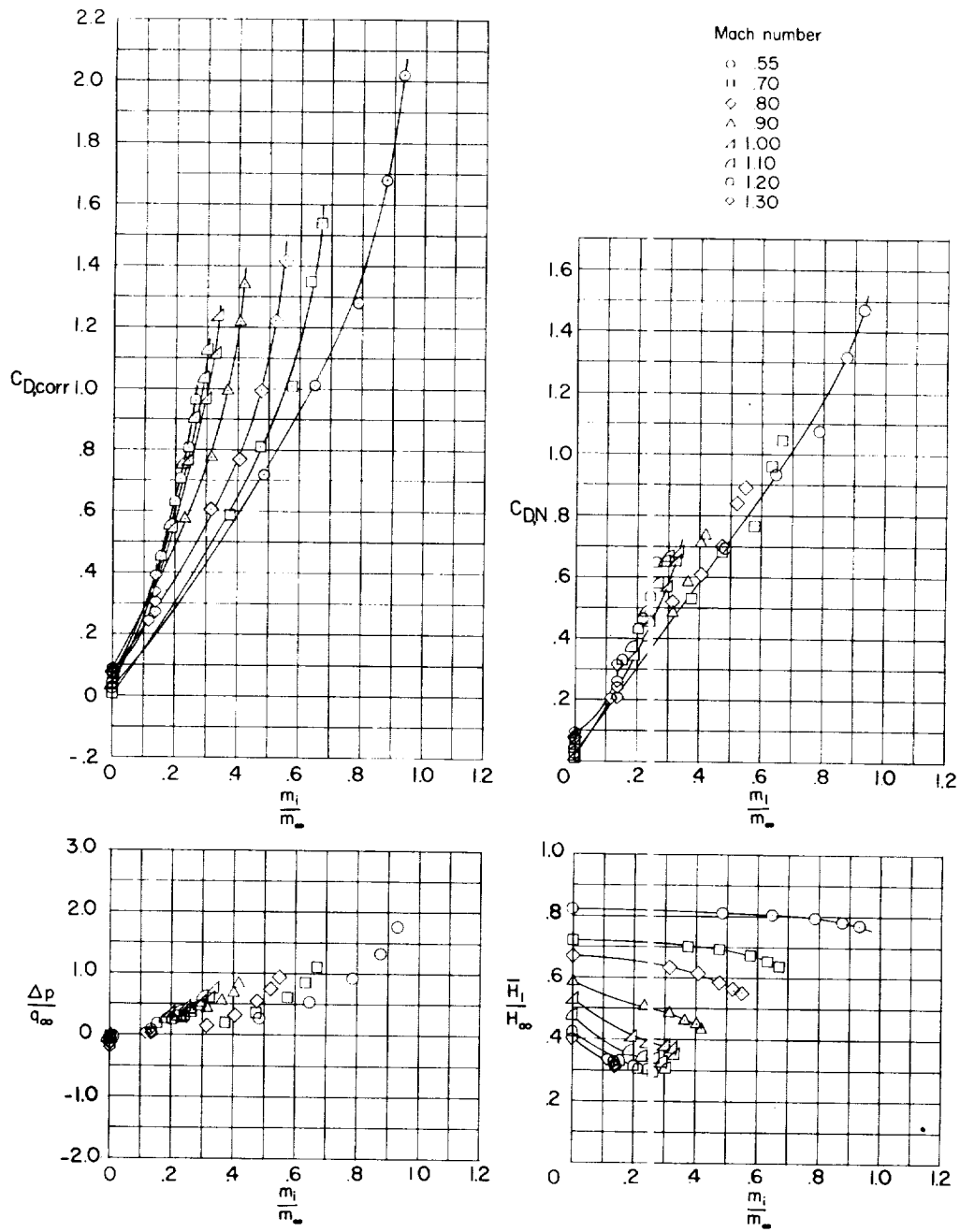
(b) $\theta = 30^\circ$.

Figure 7.- Continued.



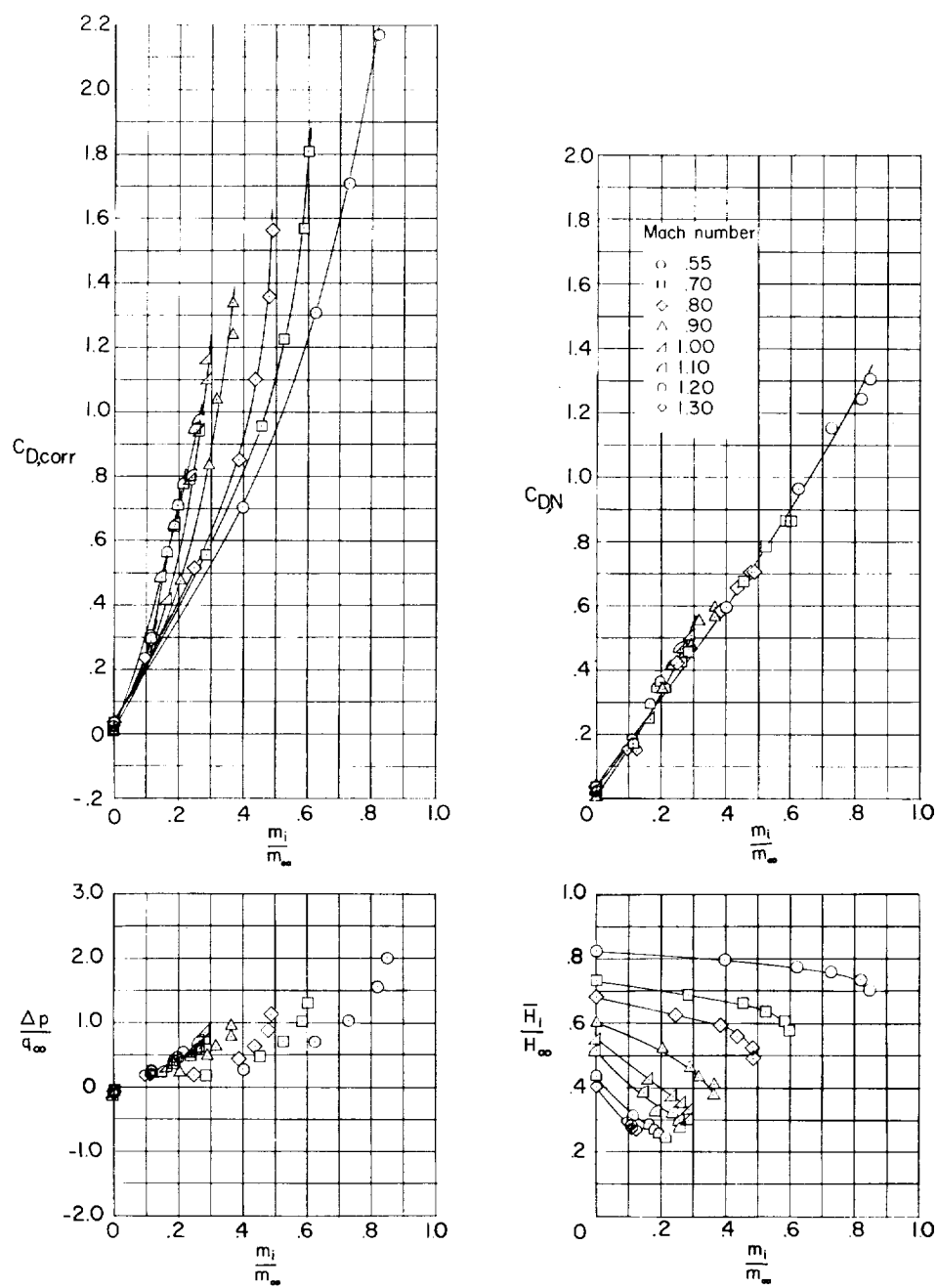
(c) $\theta = 45^\circ$.

Figure 7.- Continued.



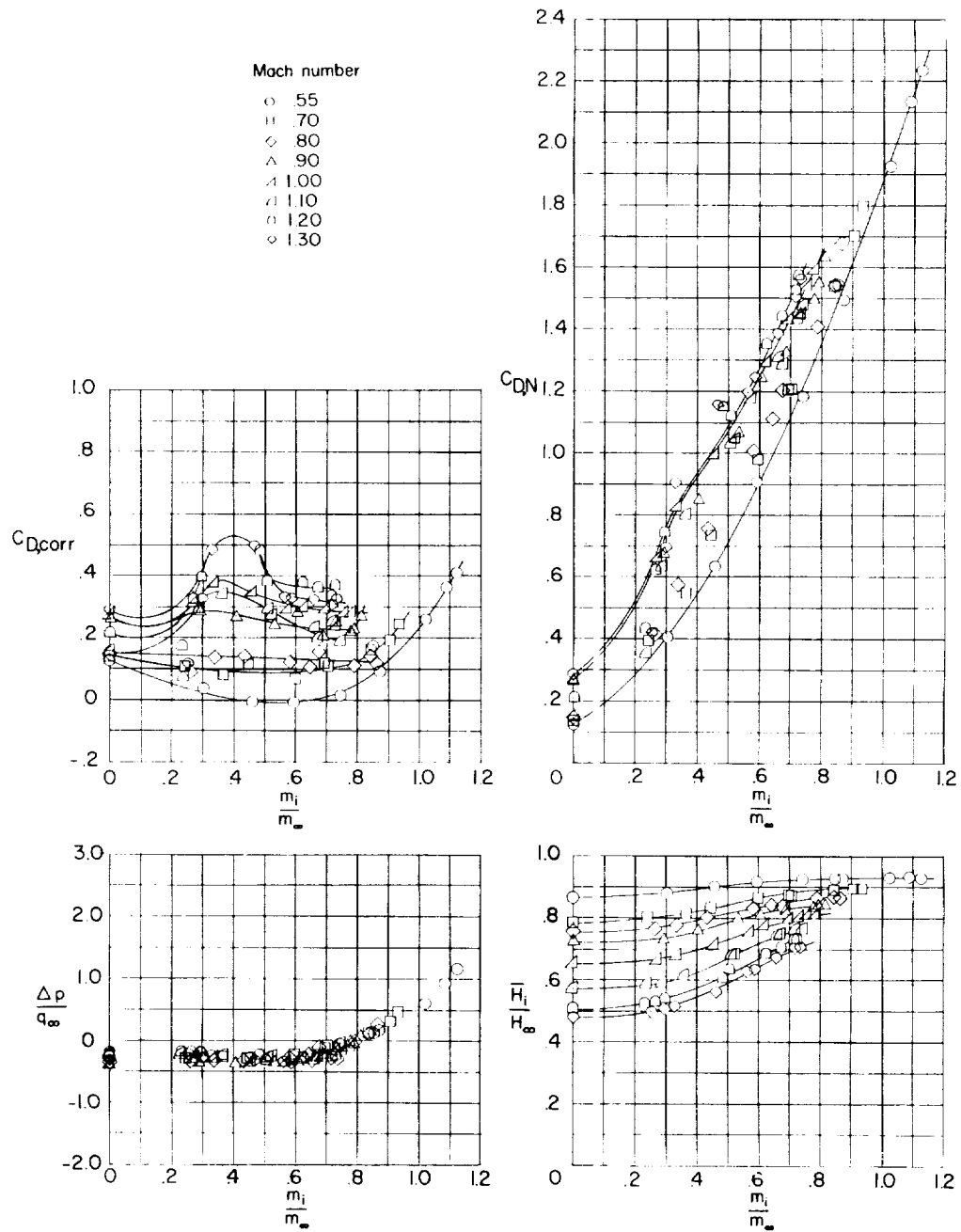
(d) $\theta = 60^\circ$.

Figure 7.- Continued.



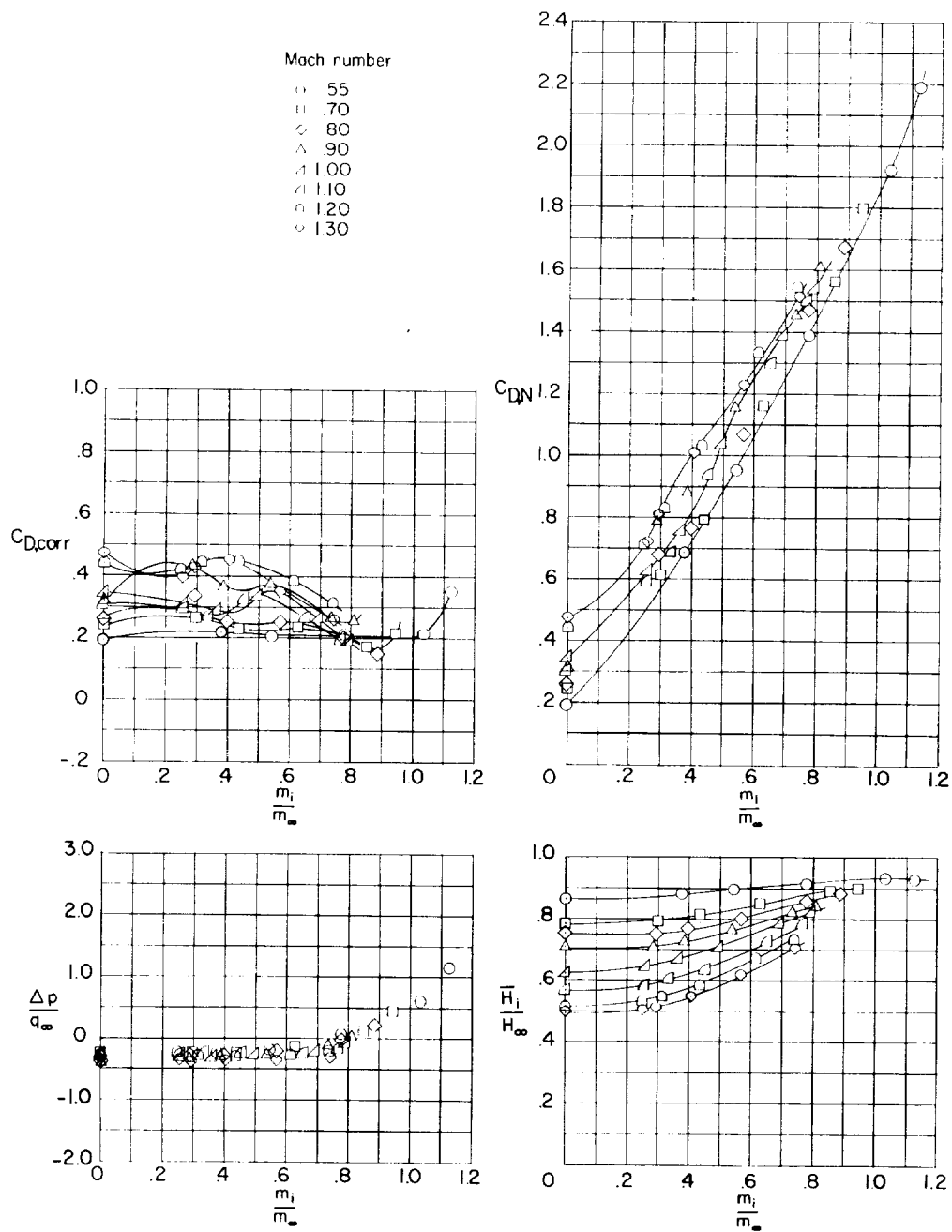
(e) $\theta = 90^\circ$.

Figure 7.- Concluded.



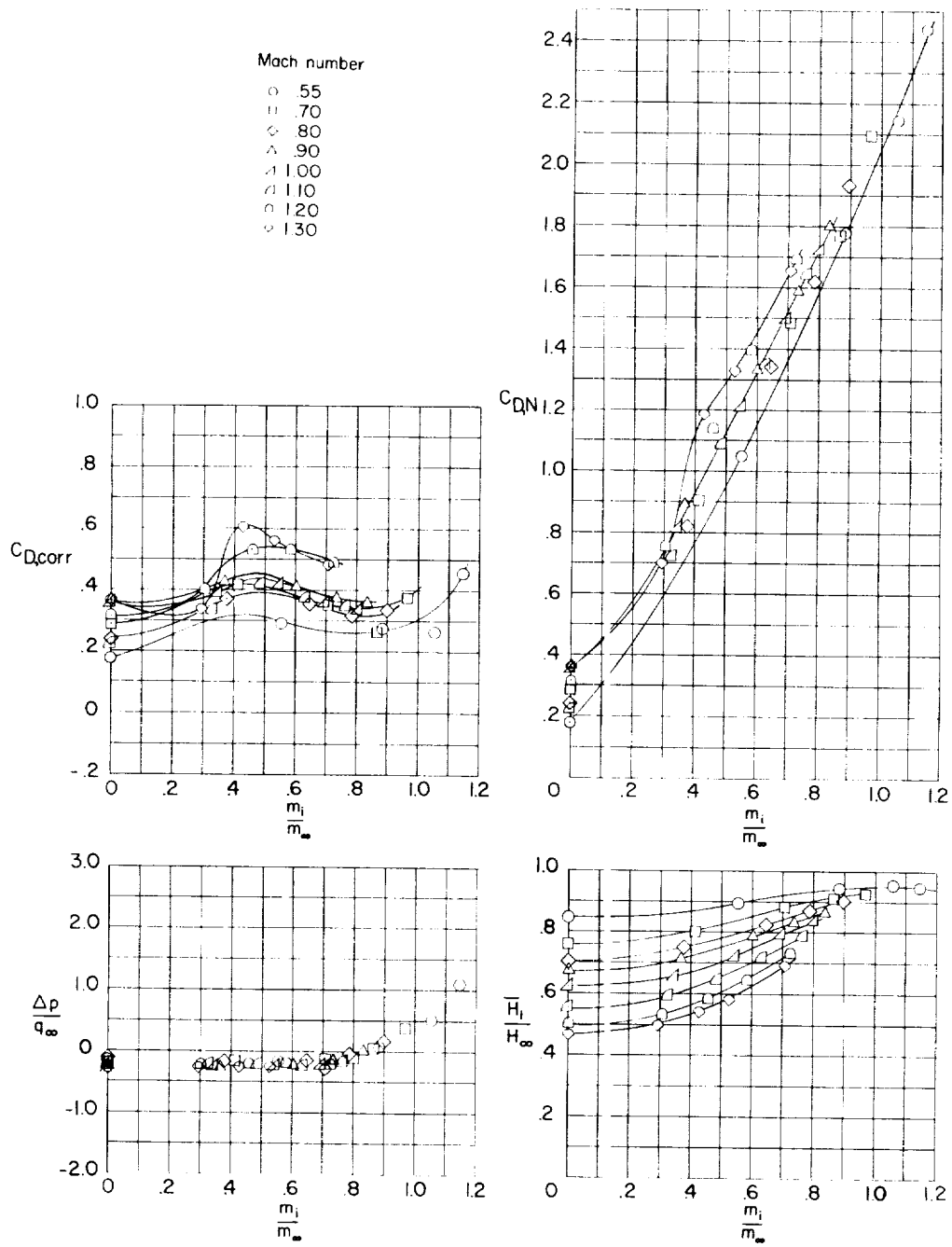
(a) Width-depth ratio, 1.

Figure 8.- Drag and pressure recovery characteristics of flush rectangular inlets of varying width-depth ratios; $\theta = 15^\circ$; $l/d = 5$.



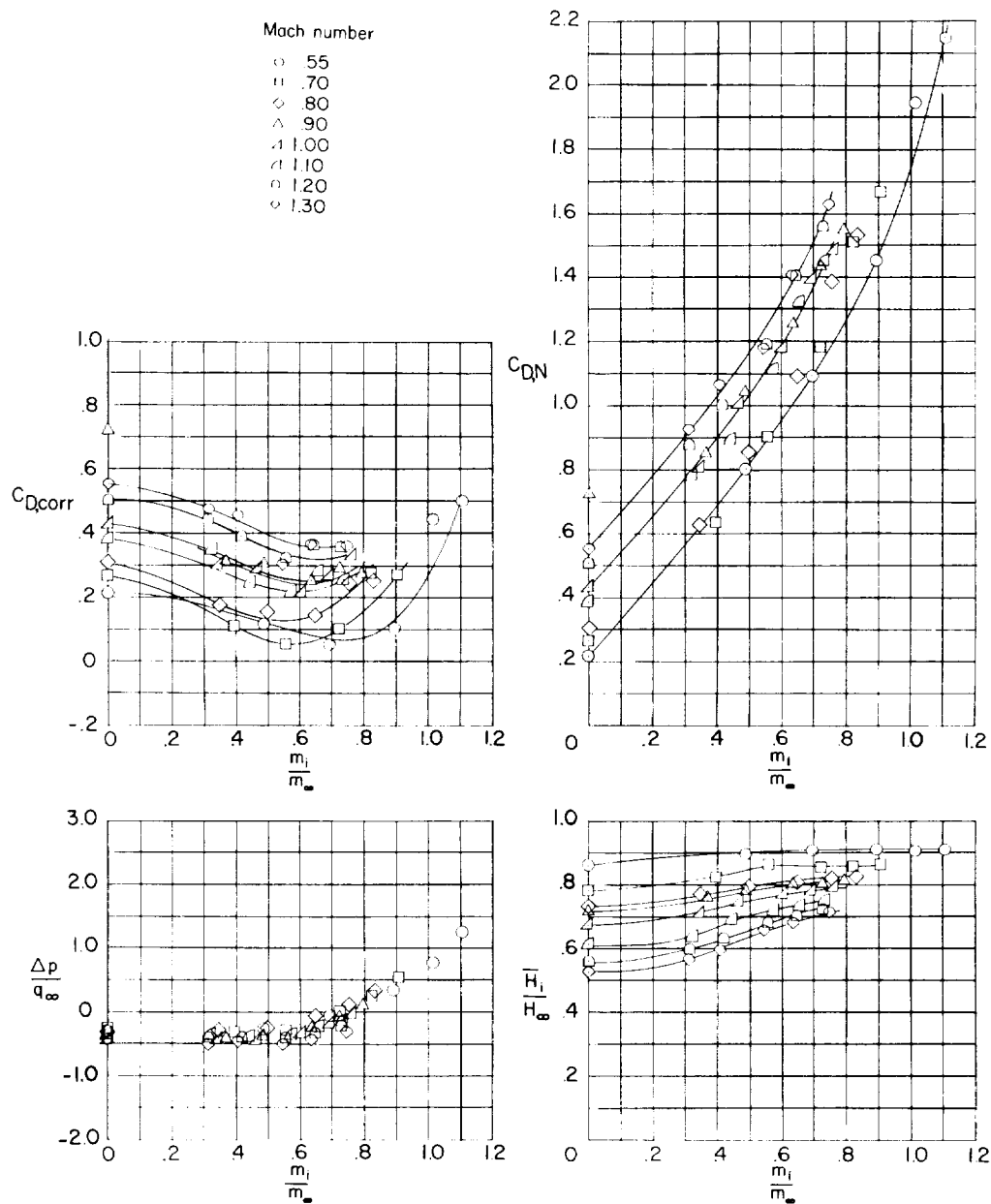
(b) Width-depth ratio, 1/4.

Figure 8.- Continued.



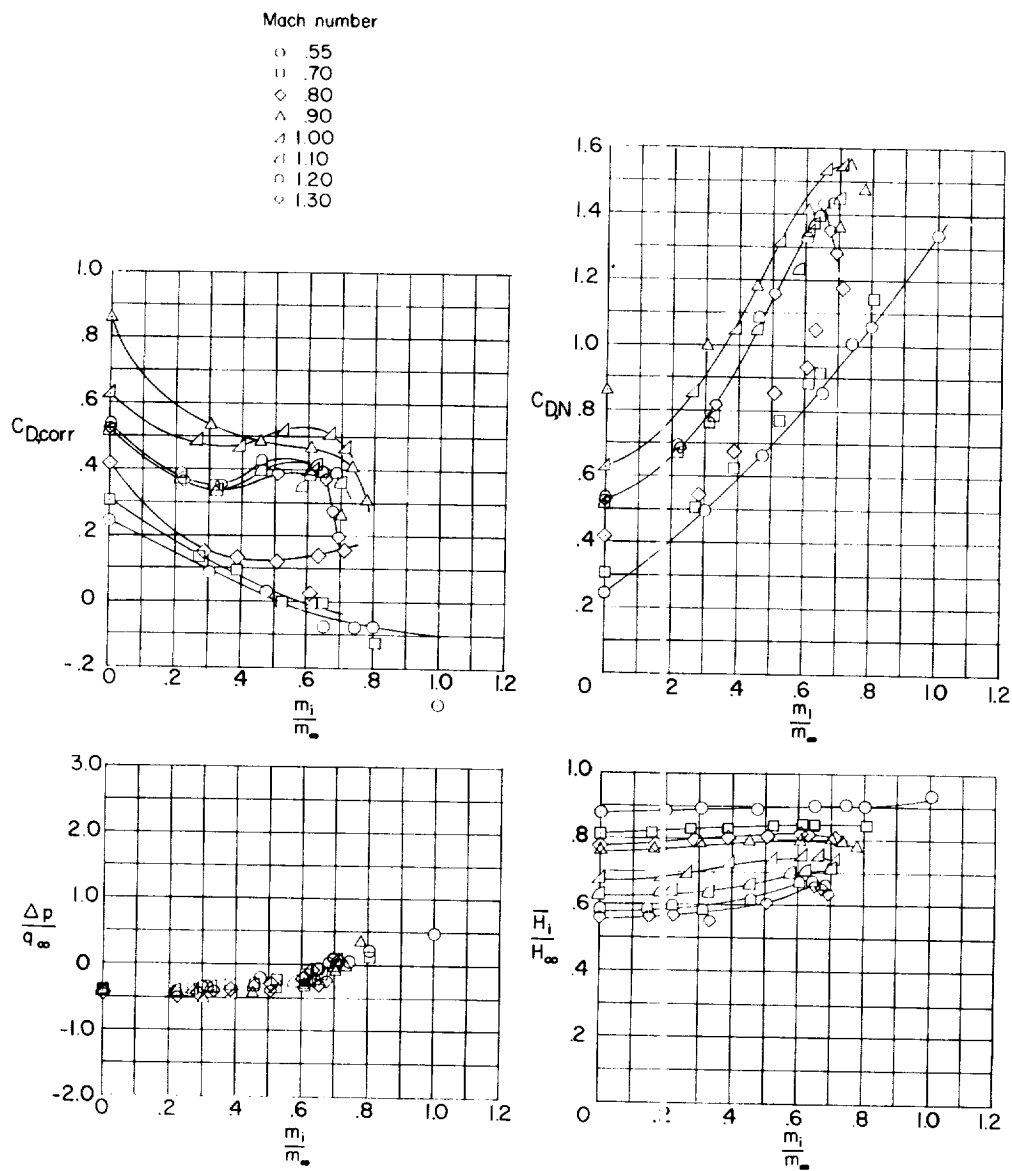
(c) Width-depth ratio, 1/4 (with fences).

Figure 8.- Concluded.



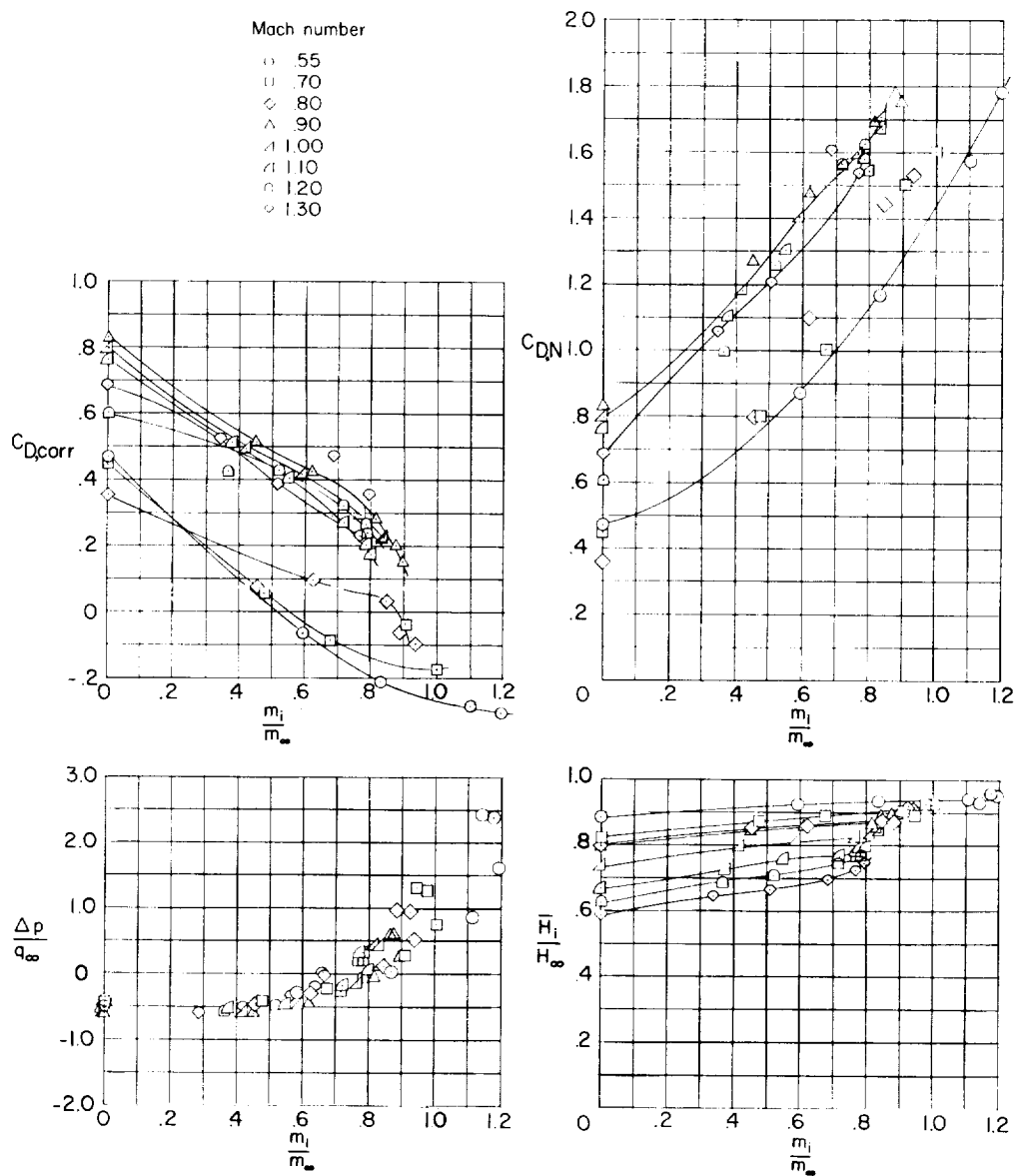
(a) Rectangular ramp; width-depth ratio, 4; $l/d = 5$.

Figure 9.- Drag and pressure recovery characteristics of flush rectangular inlets using a 7° approach ramp. $\theta = 15^\circ$.



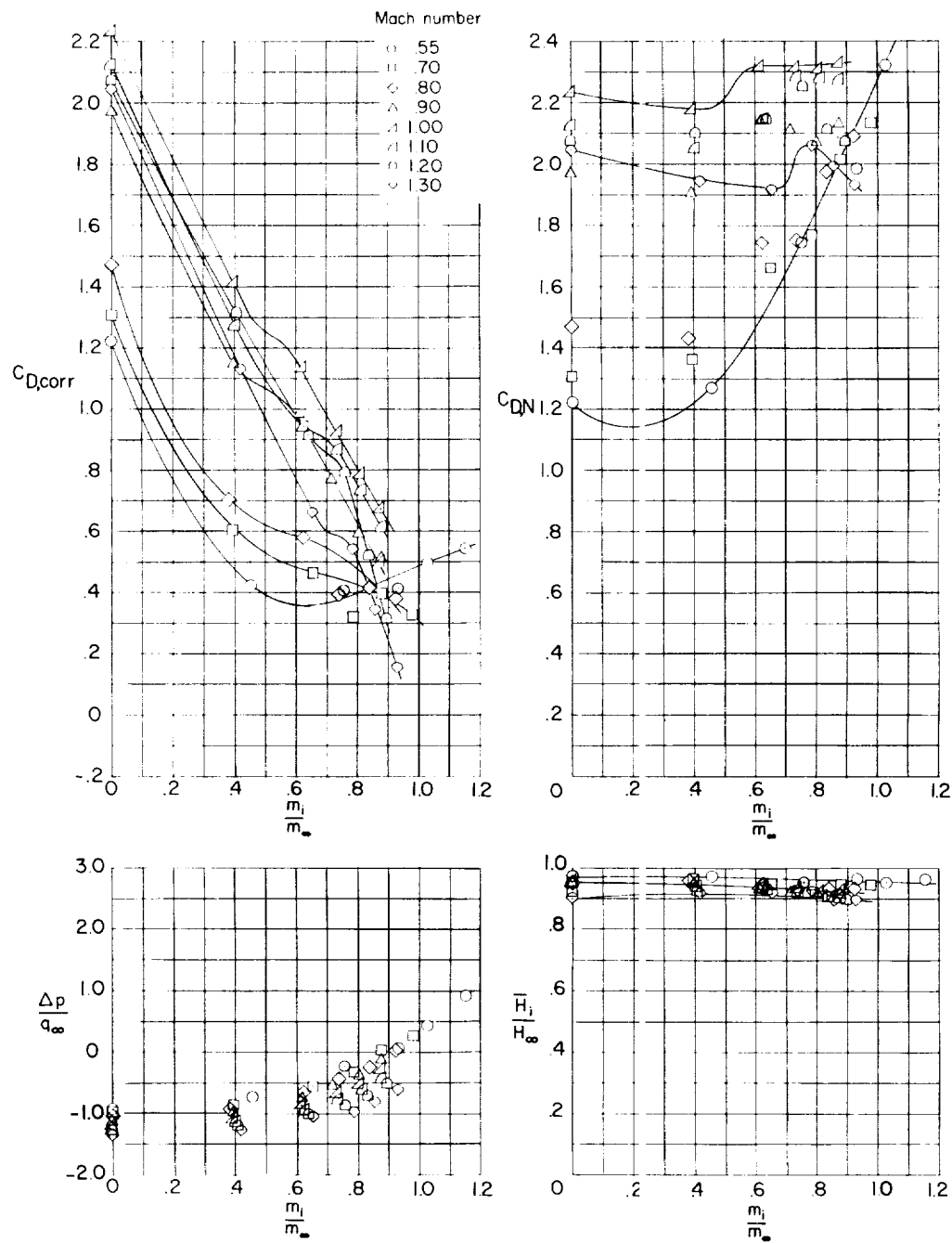
(b) Diverging-wall ramp; width-depth ratio, 4; $l/d = 5$.

Figure 9.- Continued.



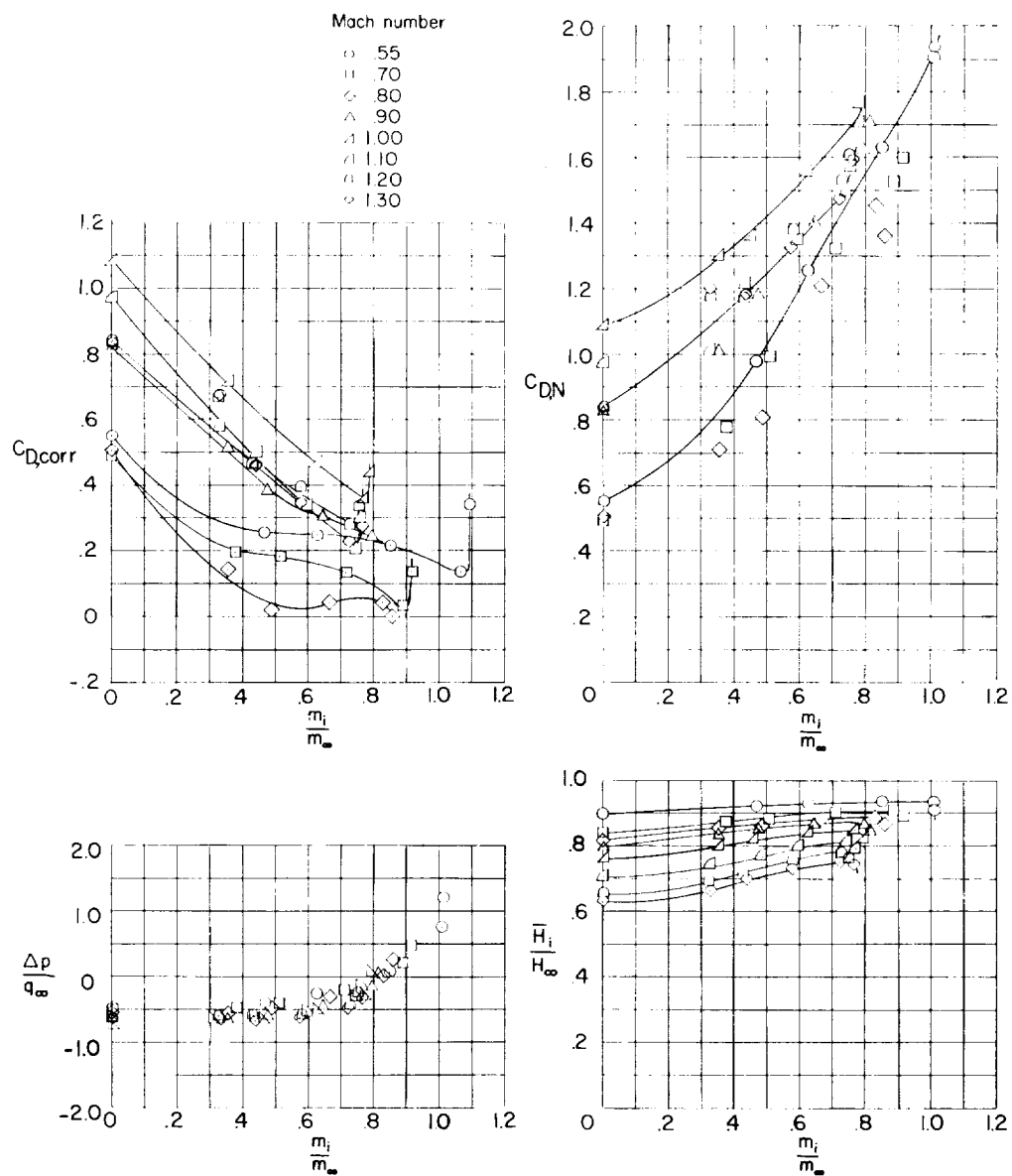
(c) Diverging-wall ramp with boundary-layer bypass; width-depth ratio, 2.51; $l/d = 5.6$.

Figure 9.- Concluded.



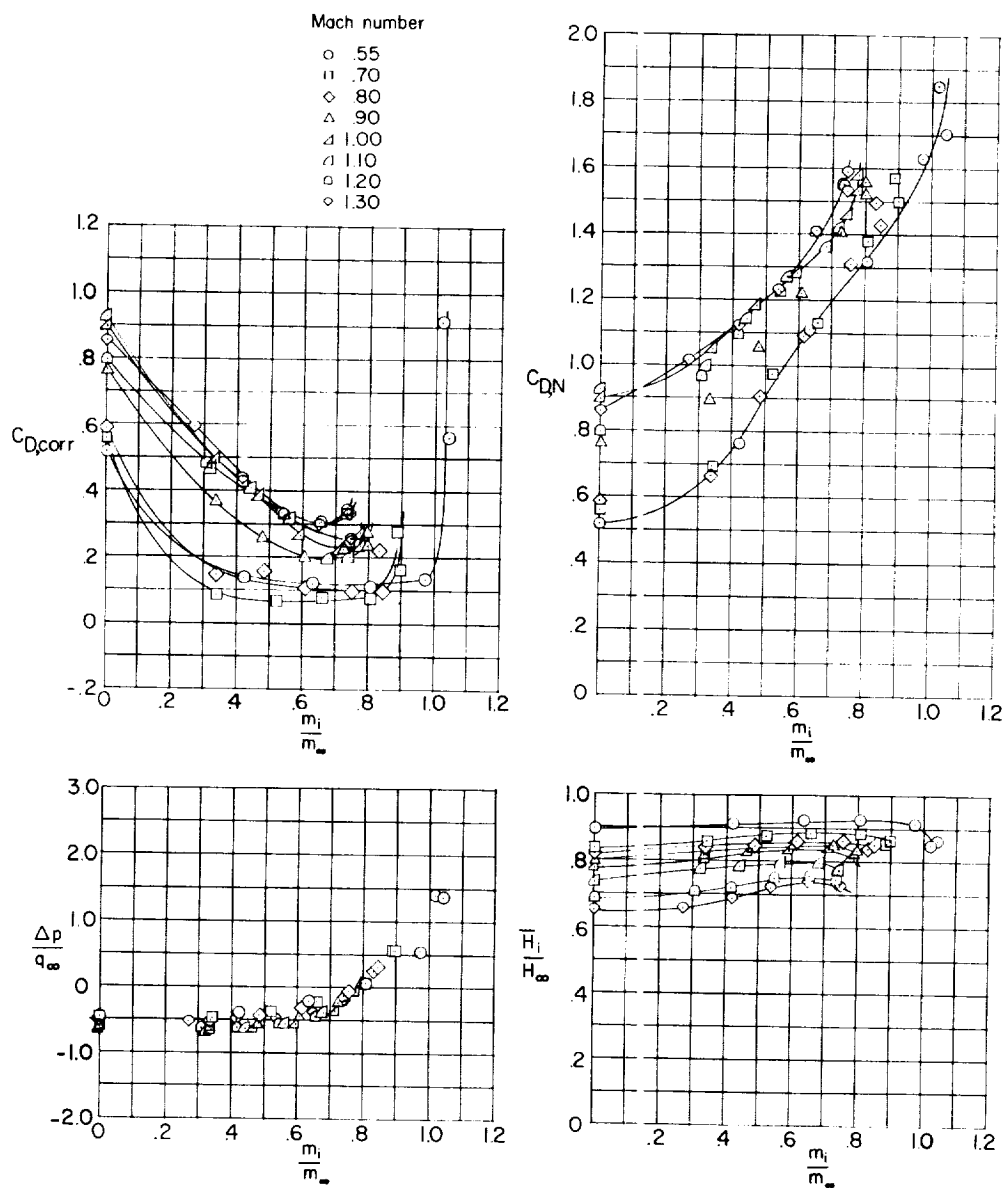
(a) Circular scoop; $\theta = 45^\circ$; $l/d = 6.8$.

Figure 10.- Drag and pressure recovery characteristics of scoop inlets.



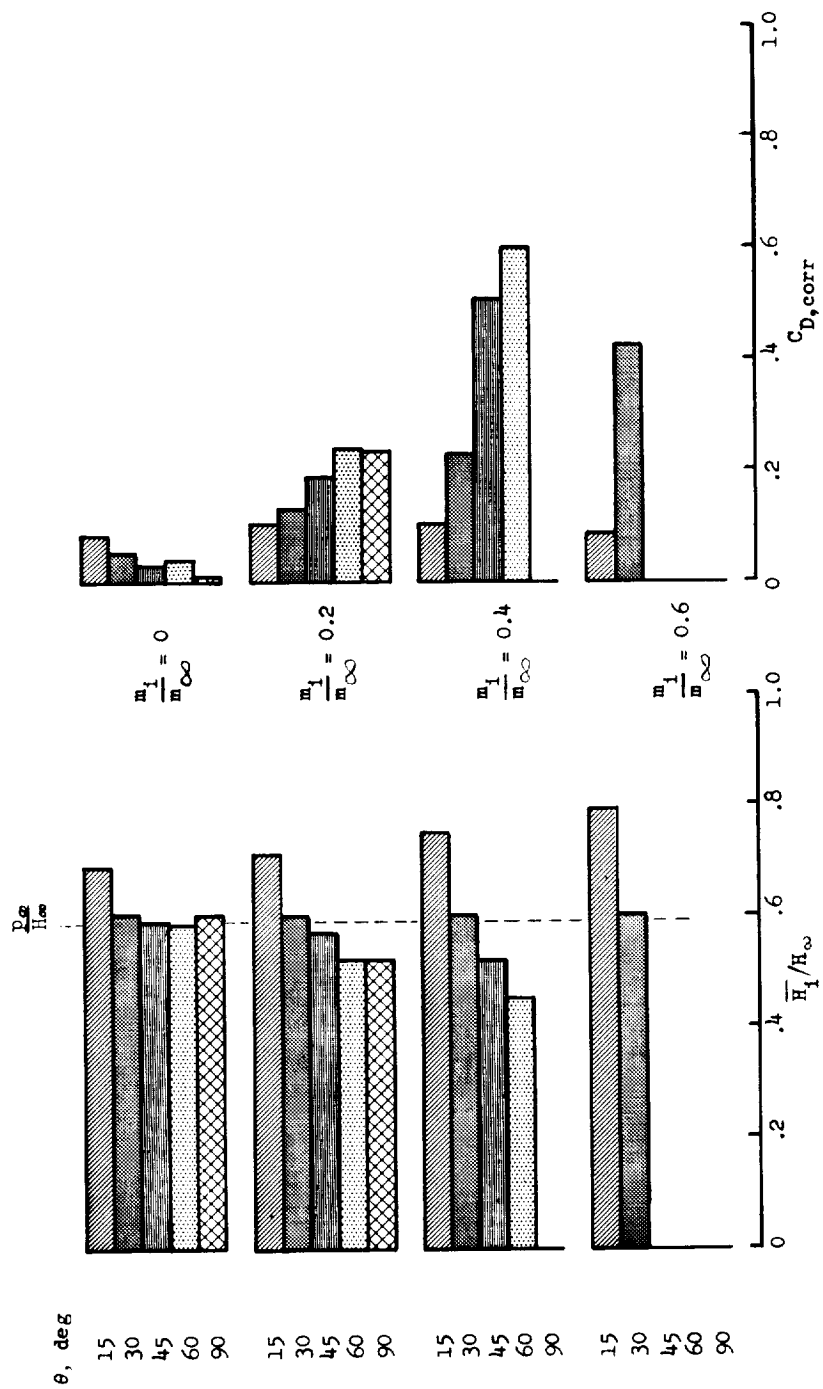
(b) Rectangular scoop; $\theta = 15^\circ$; $l/d = 6.78$; width-depth ratio, 4.

Figure 10.- Continued.



(c) Rectangular scoop; $\theta = 90^\circ$; $l/d = 5.63$; width-depth ratio, 4.

Figure 10.- Concluded.



(a) Flush rectangular inlets; variable θ ; $M_\infty = 0.9$.

Figure 11.- Bar graphs of total-pressure ratios and drag coefficients at several mass-flow ratios.

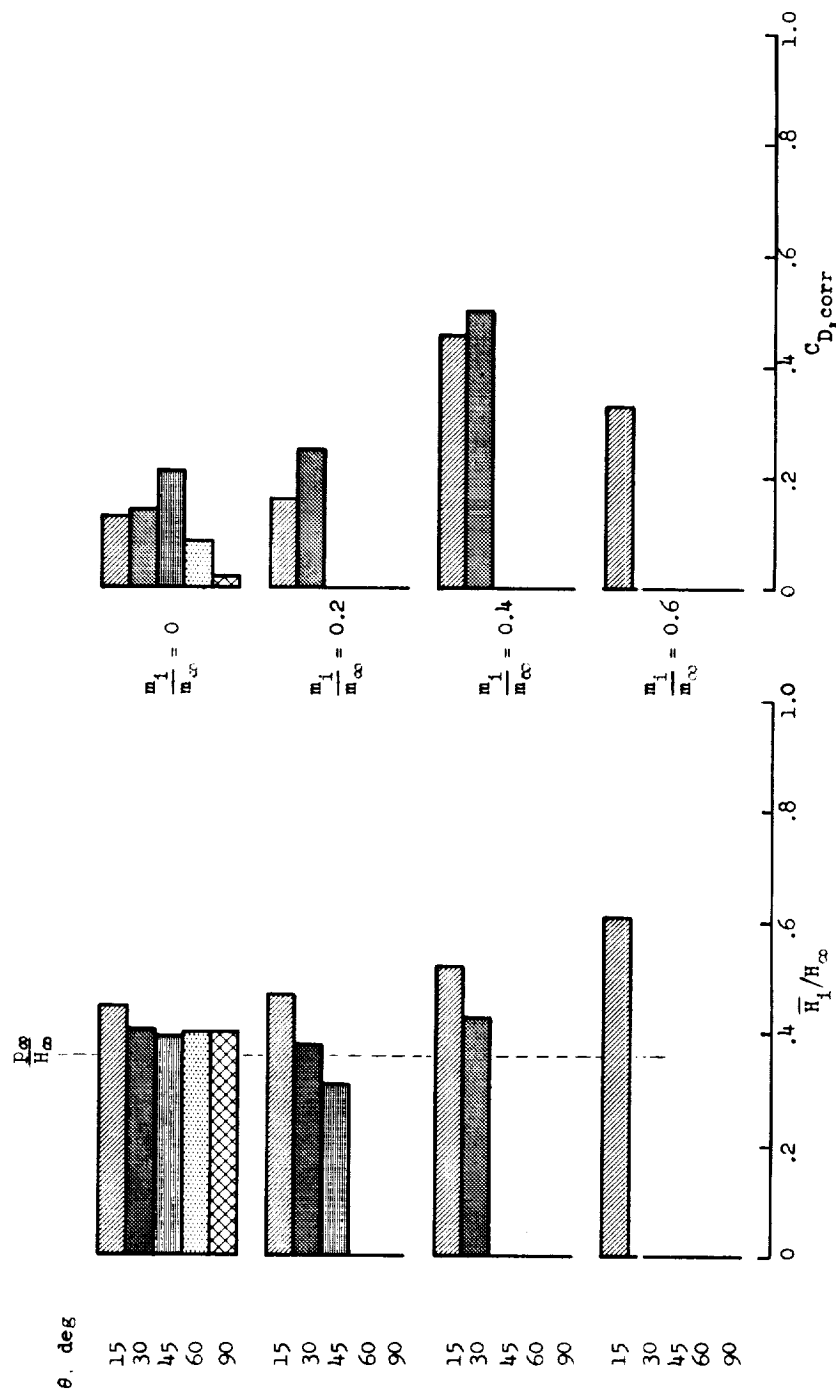
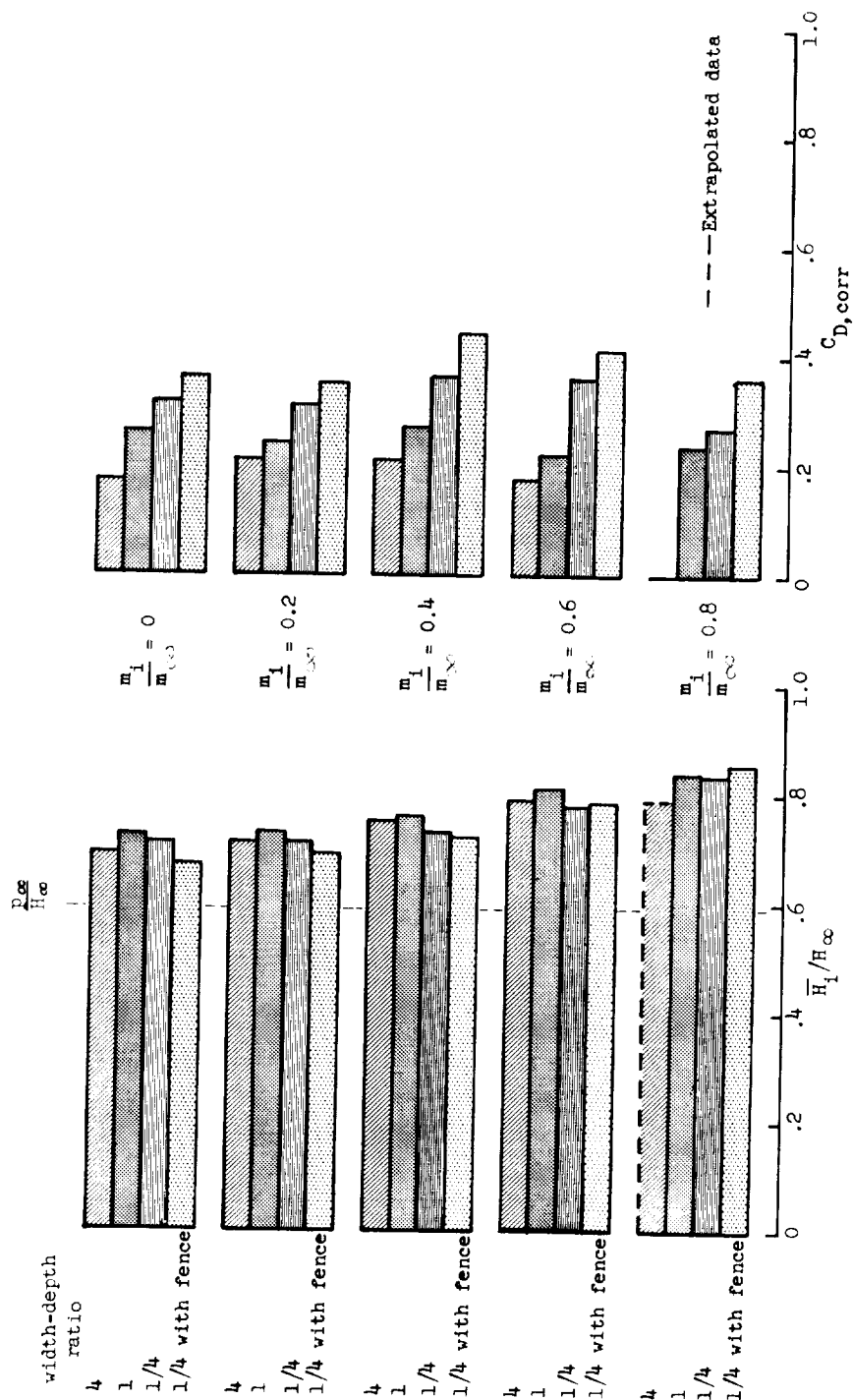
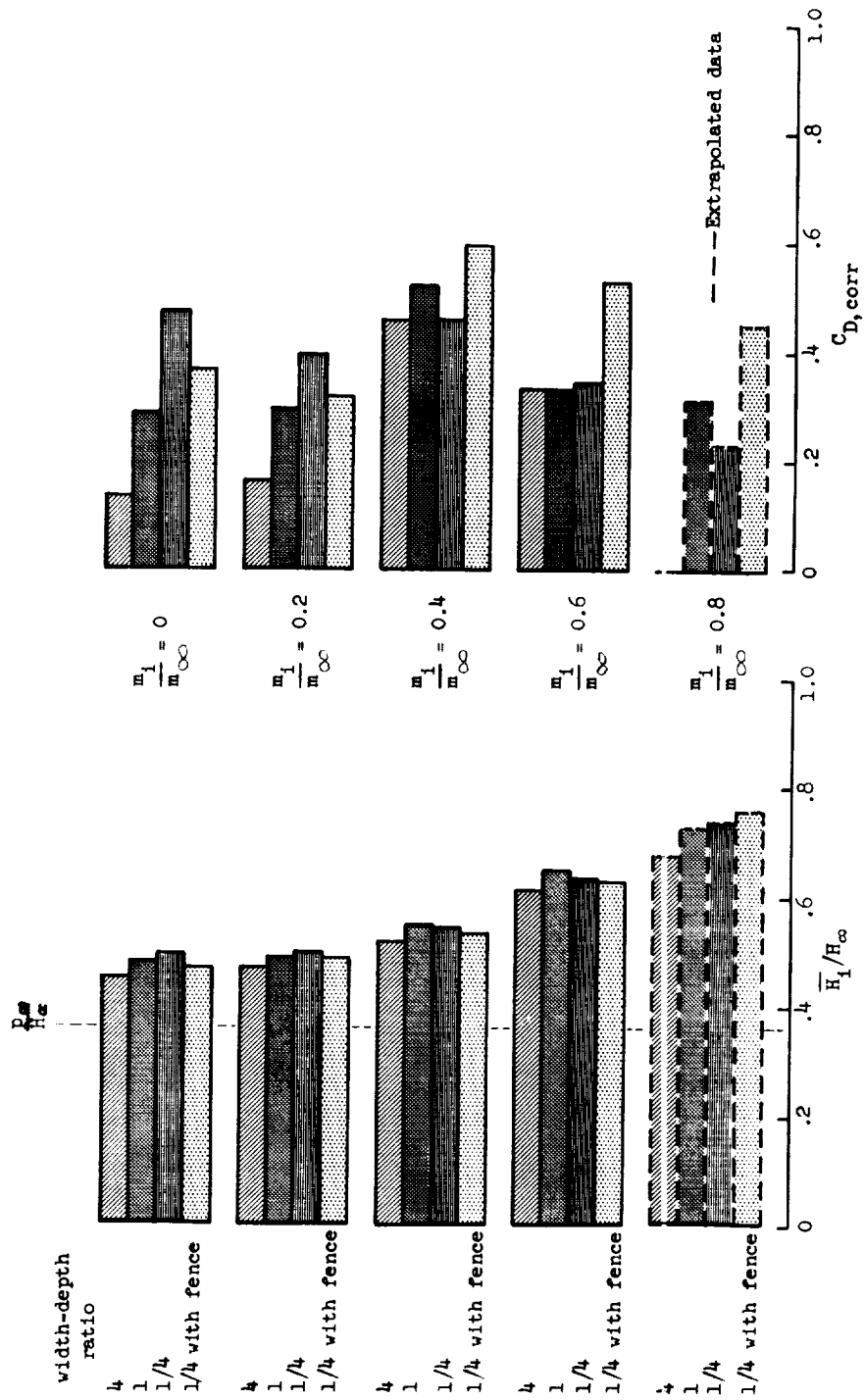


Figure 11.- Continued.



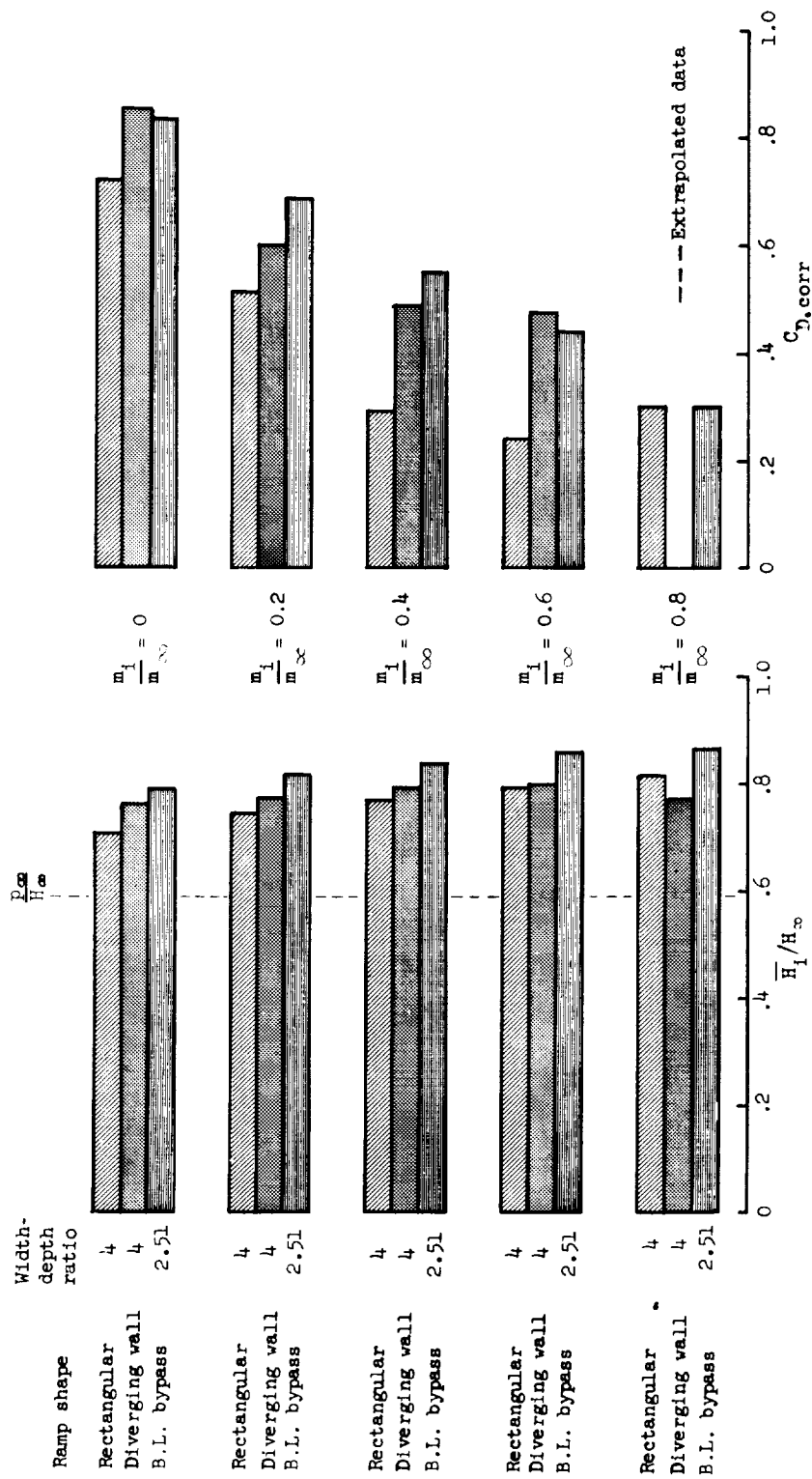
(c) Flush rectangular inlets; $\theta = 15^\circ$; variable width-depth ratio; $M_\infty = 0.9$.

Figure 11.- Continued.



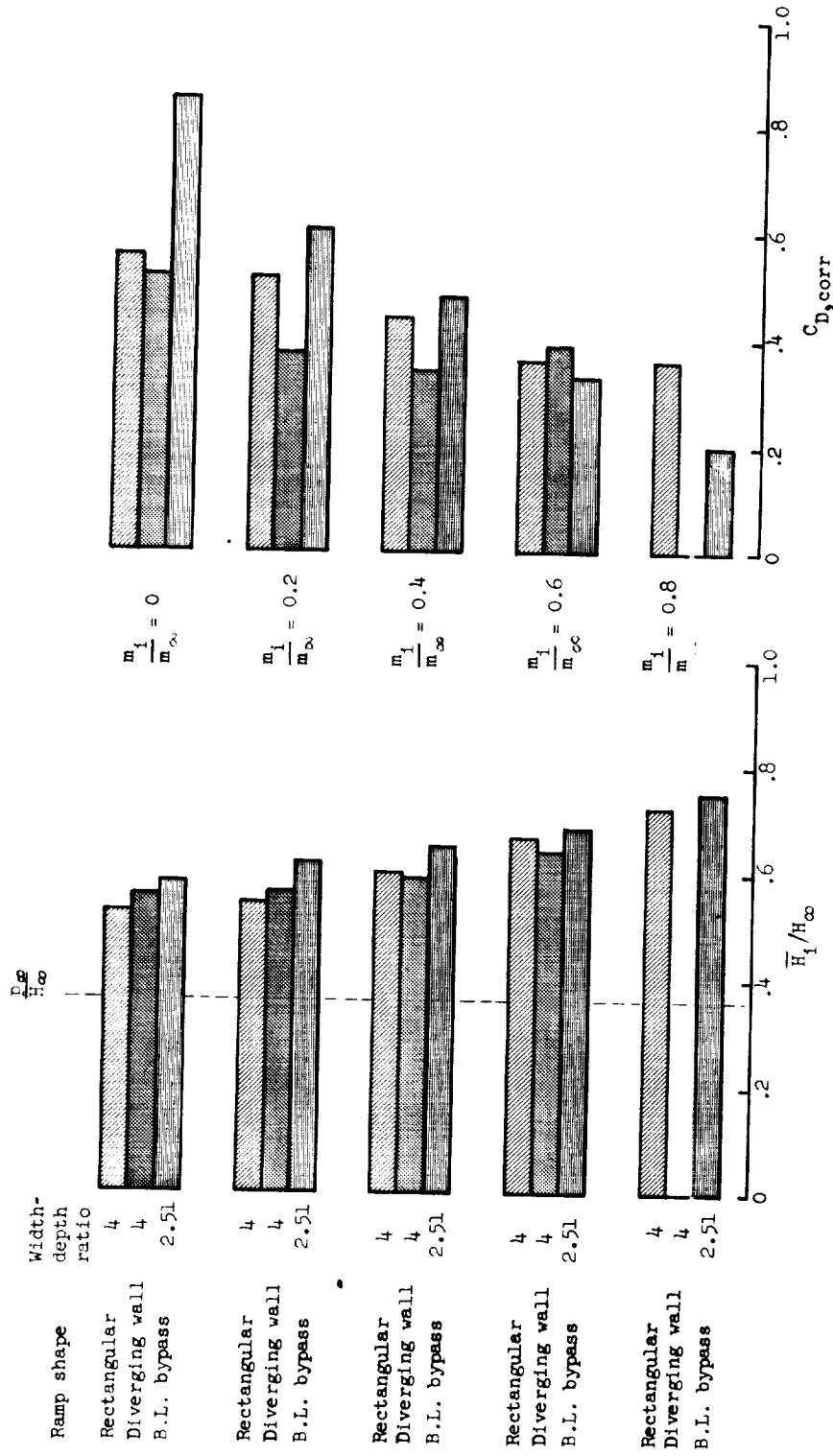
(d) Flush rectangular inlets; $\theta = 15^\circ$; variable width-depth ratio; $M_\infty = 1.3$.

Figure 11.- Continued.



(e) Flush inlets; $\theta = 15^\circ$; $\phi = 7^\circ$; variable ramp shape; $M_\infty = 0.9$.

Figure 11.- Continued.



(f) Flush inlets; $\theta = 15^\circ$; $\phi = 7^\circ$; variable ramp shape; $M_\infty = 1.3$.

Figure 11.- Continued.

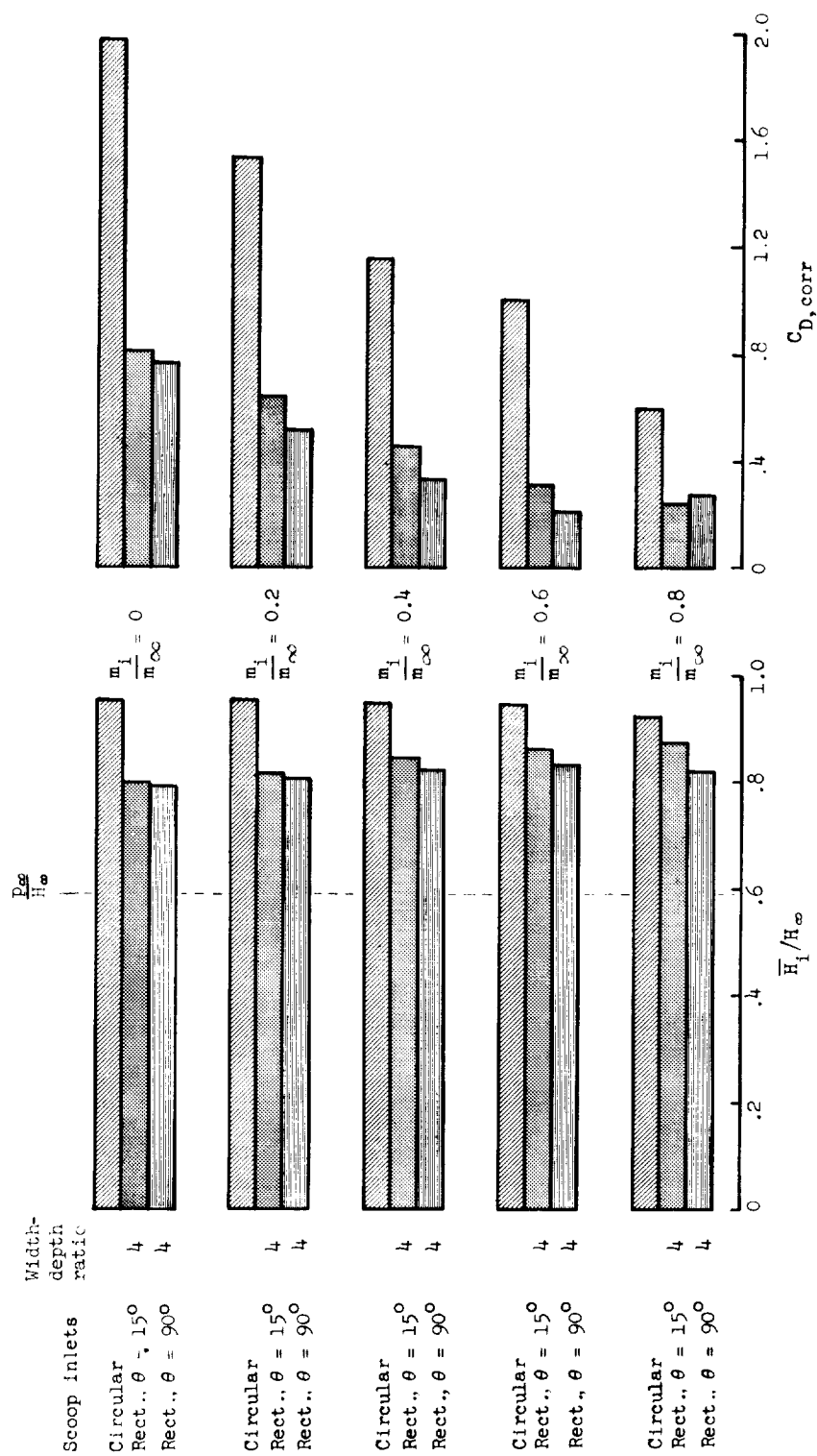
(g) Scoop inlets; $M_\infty = 0.9$.

Figure 11.- Continued.

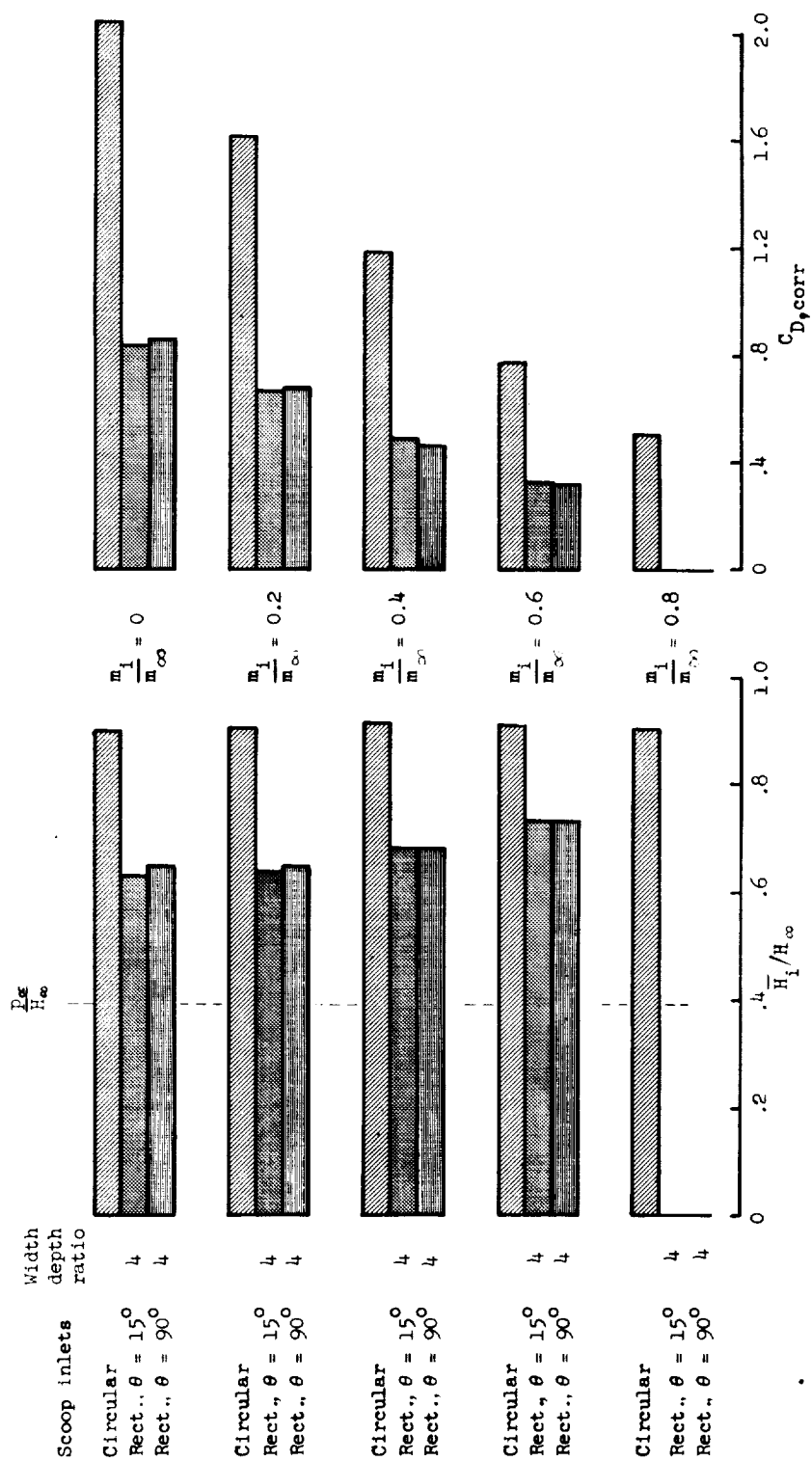
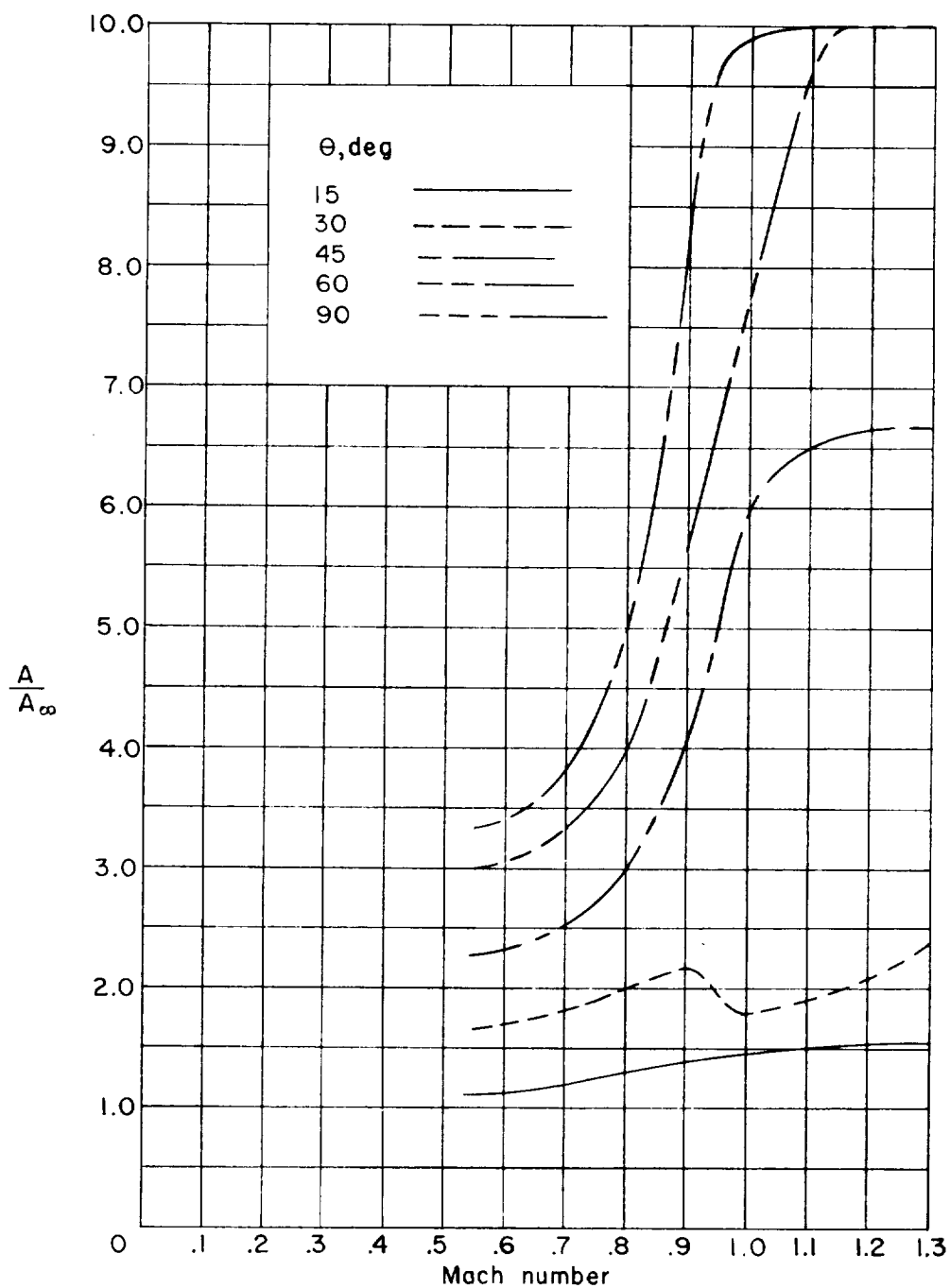
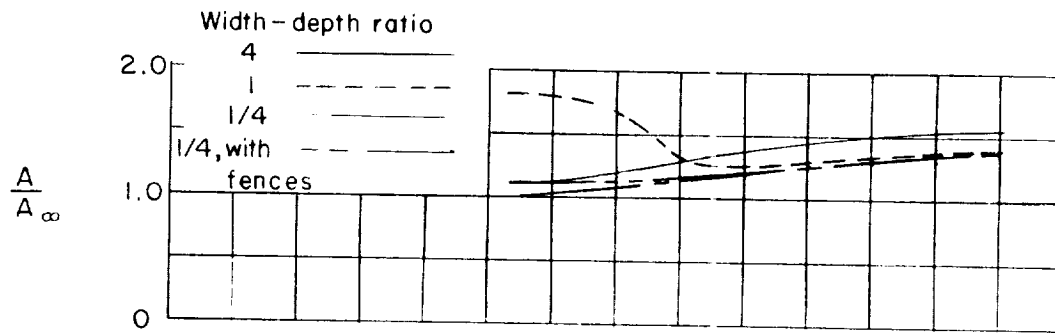
(h) Scoop inlets; $M_\infty = 1.3$.

Figure 11.- Concluded.

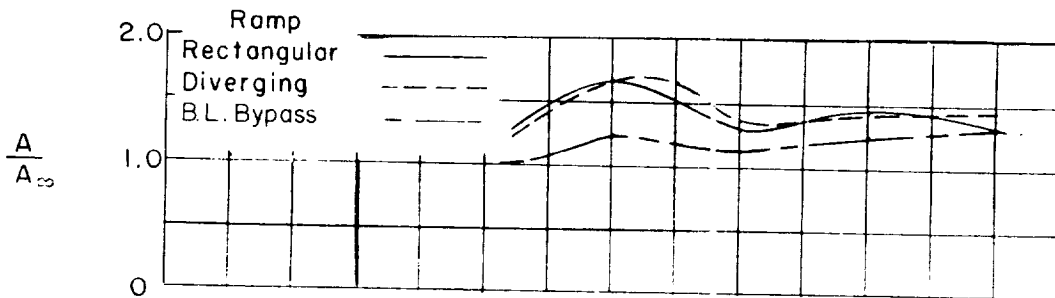


(a) Flush rectangular inlets; varying θ .

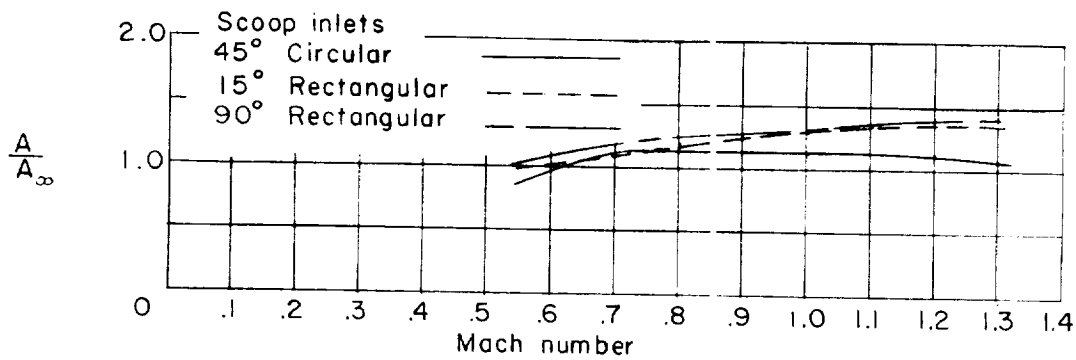
Figure 12.- Variation of required inlet area with Mach number for operation at equal mass flows and minimum drag for each inlet.



(b) Flush rectangular inlets; varying width-depth ratio; $\theta = 15^\circ$.

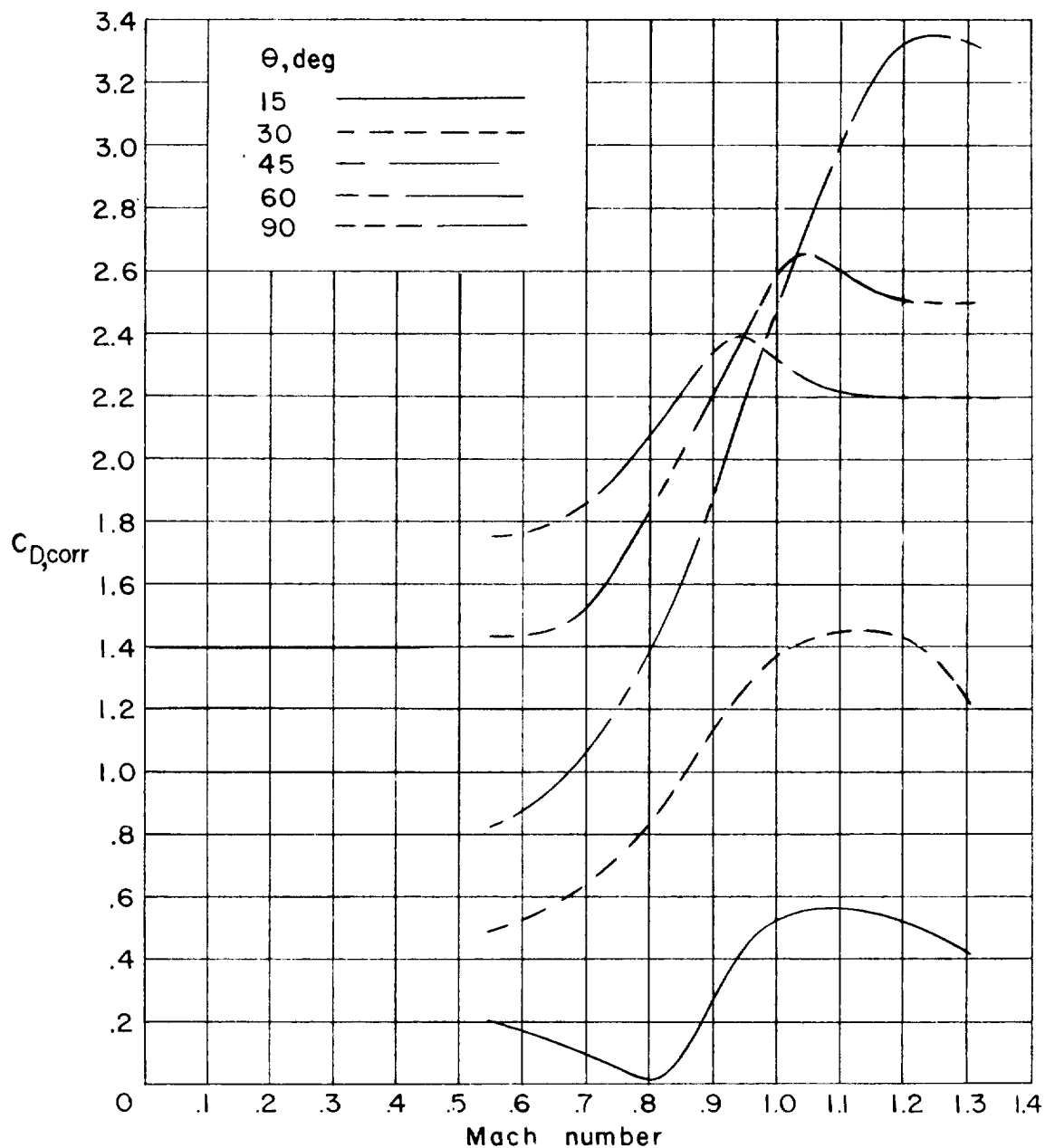


(c) Flush rectangular inlets; $\phi = 7^\circ$; varying ramp details; $\theta = 15^\circ$.



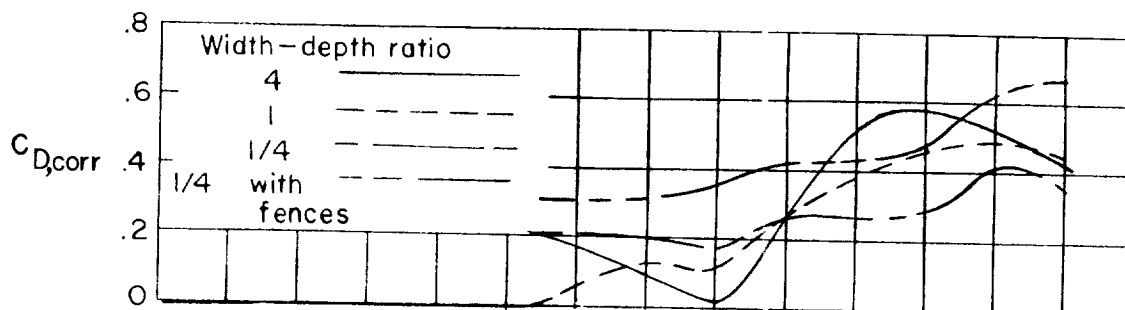
(d) Scoop inlets.

Figure 12.- Concluded.

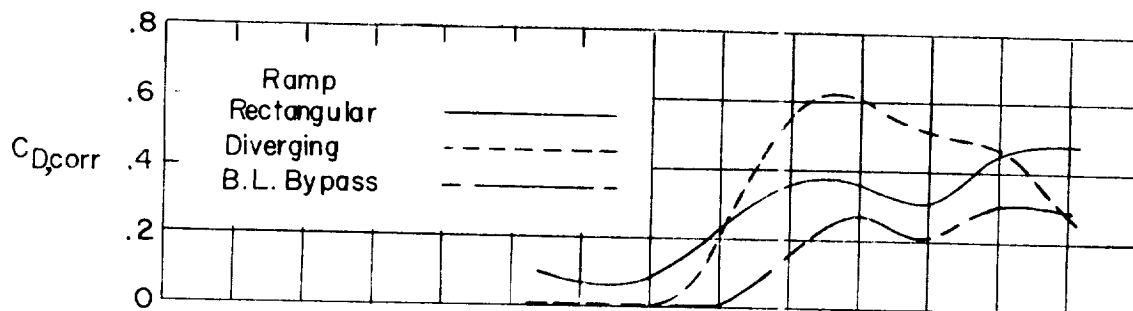


(a) Flush rectangular inlets; varying θ .

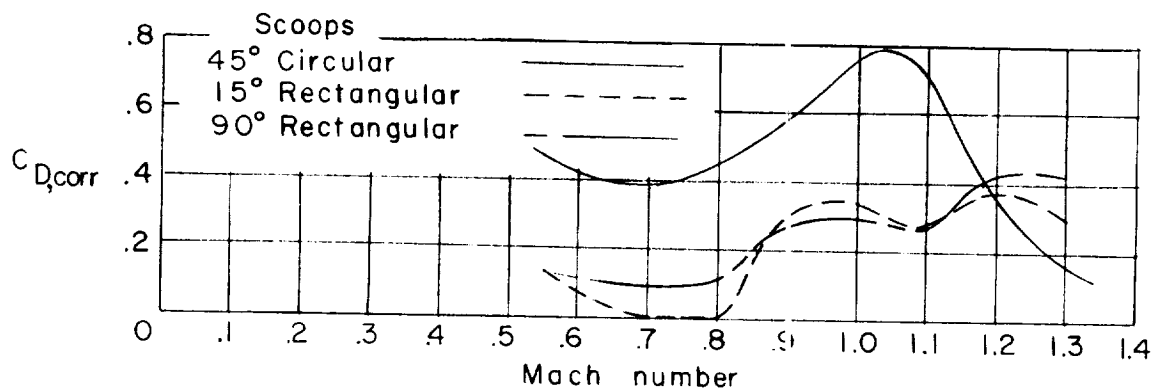
Figure 13.- Variation of minimum drag with Mach number for operation at equal mass flows for each inlet.



(b) Flush rectangular inlets; varying width-depth ratio.



(c) Flush rectangular inlets; $\phi = 7^\circ$; varying ramp details.

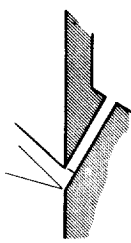
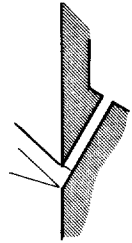
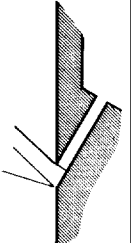
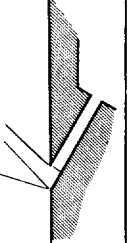


(d) Scoop inlets.

Figure 13.- Concluded.

NOTES: (1) Reynolds number is based on the diameter of a circle with the same area as that of the capture area of the inlet.

(2) The symbol * denotes the occurrence of buzz.

Report and facility	Description		Test parameters					Test data				Performance		Remarks
			Number of oblique shocks	Type of boundary-layer control	Free-stream Mach number	Reynolds number $\times 10^{-6}$	Angle of attack, deg	Angle of yaw, deg	Inlet-flow profile	Discharge-flow profile	Flow picture	Maximum total-pressure recovery	Mass-flow ratio	
CONFID. NASA MEMO 12-21-56L Langley Internal Aero Branch			Normal	None	0.55 to 1.30	0.122 to .247	0	0	✓		✓	0.95 to .74	0 to choke	Geometric variables include inlet inclination, inlet width-depth-ratio, and ramp plan form.
CONFID. NASA MEMO 12-21-56L Langley Internal Aero Branch			Normal	None	0.55 to 1.30	0.122 to .247	0	0	✓		✓	0.95 to .74	0 to choke	Geometric variables include inlet inclination, inlet width-depth-ratio, and ramp plan form.
CONFID. NASA MEMO 12-21-56L Langley Internal Aero Branch			Normal	None	0.55 to 1.30	0.122 to .247	0	0	✓		✓	0.95 to .74	0 to choke	Geometric variables include inlet inclination, inlet width-depth-ratio, and ramp plan form.
CONFID. NASA MEMO 12-21-56L Langley Internal Aero Branch			Normal	None	0.55 to 1.30	0.122 to .247	0	0	✓		✓	0.95 to .74	0 to choke	Geometric variables include inlet inclination, inlet width-depth-ratio, and ramp plan form.

Bibliography

These strips are provided for the convenience of the reader and can be removed from this report to compile a bibliography of NASA inlet reports. This page is being added only to inlet reports and is on a trial basis.

